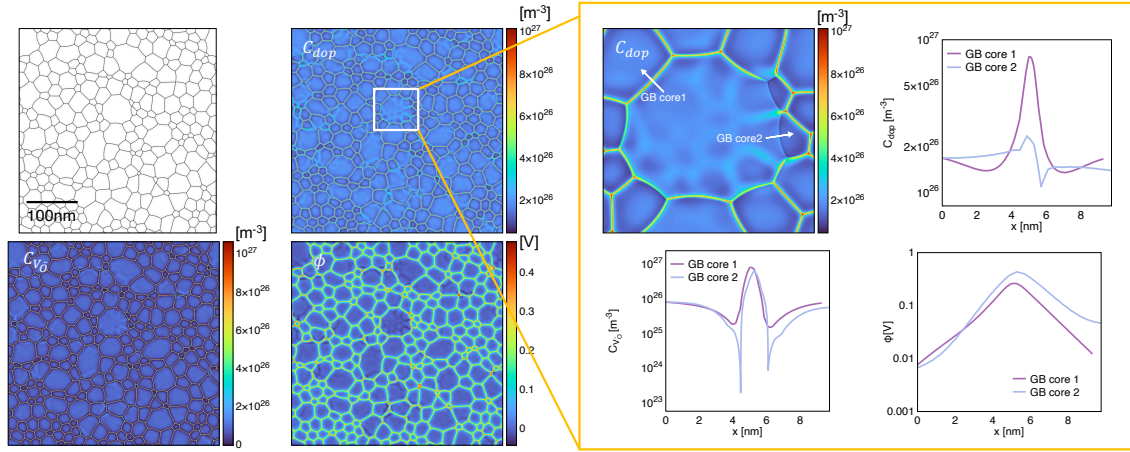


# Graphical Abstract

## A defect-chemistry-informed phase-field model of grain growth in oxide electroceramics

Kai Wang, Roger A. De Souza, Xiang-Long Peng, Rotraut Merkle, Wolfgang Rheinheimer, Karsten Albe, Bai-Xiang Xu



# A defect-chemistry-informed phase-field model of grain growth in oxide electroceramics

Kai Wang<sup>a</sup>, Roger A. De Souza<sup>b</sup>, Xiang-Long Peng<sup>a</sup>, Rotraut Merkle<sup>c</sup>, Wolfgang Rheinheimer<sup>d</sup>,  
Karsten Albe<sup>e</sup>, Bai-Xiang Xu<sup>a,\*</sup>

<sup>a</sup>*Mechanics of Functional Materials Division, Institute of Materials Science, Technische Universität Darmstadt, Darmstadt, 64287, Germany*

<sup>b</sup>*Institute of Physical Chemistry, RWTH Aachen University, Aachen, 52056, Germany*

<sup>c</sup>*Max Planck Institute for Solid State Research, Heisenbergstraße 1, Stuttgart, 70569, Germany*

<sup>d</sup>*University of Stuttgart, Institute for Manufacturing Technologies of Ceramic Components and Composites (IFKB), Stuttgart, 70569, Germany*

<sup>e</sup>*Materials Modelling Division, Institute of Materials Science, Technische Universität Darmstadt, Darmstadt, 64287, Germany*

---

## Abstract

Dopants can significantly affect the properties of oxide ceramics through their impact on the property-determined microstructure characteristics such as grain boundary segregation, space charge layer formation in the grain boundary vicinity, and the resultant microstructure features like bimodality due to abnormal grain growth. To support rational oxide ceramics design, we propose a multiphysics-based and defect-chemistry-informed phase-field grain growth model to simulate the microstructure evolution of oxide ceramics. It fully respects the thermodynamics of charged point defects (oxygen vacancies and dopants) in both the grain interior and boundaries and considers the competing kinetics of defect diffusion and grain boundary movement. The proposed phase-field model is benchmarked against well-known simplified bicrystal models, including the Mott-Schottky and Gouy-Chapman models. Various simulation results are presented to reveal the impacts of defect formation energy differences between the grain interior and the grain boundary core on the key microstructural aspects. In particular, simulation results confirm that the solute drag effect alone can lead to bimodal grain size distribution, without any contribution from grain misorientation and other anisotropy. Interestingly, abnormal grain growth simulations demonstrate that grain boundary potentials can vary substantially: grain boundaries of larger grains tend to have lower potentials than those of smaller grains. Such heterogeneous grain boundary potential distribution may inspire a new material optimization strategy through microstructure design. This study provides a comprehensive framework for defect-chemistry-consistent investigations of microstructure evolution in polycrystalline oxide ceramics, offering fundamental insights into in-situ processes during critical manufacturing stages.

**Keywords:** Phase-field method, Defect-chemistry, Space charge layer, Abnormal grain growth

---

---

\*Corresponding author



## 1. Introduction

In recent decades, oxide ceramics, such as  $\text{SrTiO}_3$  (STO) and  $\text{BaTiO}_3$  (BTO), have undergone tremendous development and are increasingly crucial in applications, such as solid oxide fuel cells [1, 2], sensors [3, 4], capacitors [5, 6], actuators [7, 8], and memristors [9, 10]. Oxide ceramics can be fabricated via sintering or deposition processes [11–14]. When manufactured through sintering, oxide ceramics exhibit a polycrystalline microstructure, with their macroscopic properties heavily influenced by the synthesis conditions [15]. To tailor the physical and chemical properties of oxide ceramics, heterovalent substitution (doping) is an effective method for introducing additional charged defects through ionic compensation during synthesis. The state-of-the-art designs are mostly empirical, since knowledge of the correlation among doping strategies, processing and the resultant microstructure is limited. The influential mechanisms of doping on microstructure in oxide ceramics are manifold. First of all, the addition of doping elements in the parent material systems triggers defect chemistry reaction and results in multiple types of charged point defects or defect complexes, which interact with the grain boundary (GB) chemically, electrically and elastically and form space charge layers (SCLs) around GB. More specifically, the equilibrium concentrations of the point defects within the bulk are thermodynamically determined through defect chemistry [16, 17]. The scenario near inside the GB core and in the GB vicinity are different. In undoped and acceptor doped perovskites such as Fe-doped STO, the GB core is positively charged with excess oxygen vacancies, notated  $V_{\text{O}}$  in Kröger-Vink notation [18], stemming from the negative formation energy difference of oxygen vacancy between GB core and bulk, i.e.  $\Delta g_{V_{\text{O}}} = \mu_{V_{\text{O}},c}^0 - \mu_{V_{\text{O}},b}^0 < 0$ . To compensate the positively charged GB core, a negatively charged region forms adjacent to it, called the space charge layer (SCL).

Sharp interface models have been used to describe the SCL and the related grain boundary potential. Among them are the Mott-Schottky (MS) model and the Gouy-Chapman (GC) model. The MS model assumes that the dopant concentration is constant, and only the oxygen vacancies are able to redistribute, in order to form the SCLs. In contrast, the GC model has both defects as mobile and thus allows both to contribute to charge compensation. Unlike oxygen vacancies, acceptor dopant forms an accumulation region within the SCL and in the GB core due to their negative charge [Fig. 1(e)]. The spatial inhomogeneity introduced by SCL formation exerts a profound impact on the transport dynamics of charge species. Evidence shows that cation diffusion parallel to the GB is expedited [19, 20], whereas charge transport across the GB is significantly hindered [21].

SCLs determine not only the GB local properties of the synthesized material, but also impact the grain growth dynamics already during the synthesis, e.g., the well-known solute drag effect. Grain growth in oxide ceramics, driven by a reduction in surface area and controlled by the diffusion of charged species, plays a crucial role in determining the final grain size distribution and the concentration distributions of various point defects. Segregation in a moving GB core necessitates additional free energy dissipation and results in the solute drag effect [22, 23]. This effect significantly interferes with the kinetics of grain growth and can independently trigger abnormal grain growth even in the absence of any texture or pinning sites [24]. Dopant segregation to GB core has been experimentally evidenced, especially at high temperatures [25, 26]. Experiments also show that even 0.2% amount of Fe in STO can pin certain portion of GBs [Fig. 1(b)]. This trend increases with 2% Fe [Fig. 1(c)]. When increasing the dopant concentration to 5% [Fig. 1(d)], the grain growth is completely suppressed [25, 27]. In addition, the grain growth coefficient is found to follow a non-Arrhenius behavior between 1350°C and 1425°C. Two types of GB core with different

mobilities are proposed to explain the non-Arrhenius behavior [25, 28]. Despite various evidence supporting the impact of SCLs on GB properties and grain growth dynamics, experimental characterization of the SCL remains a challenge [29]. The complexity arises from the inherent structural and compositional heterogeneities present in polycrystalline oxide ceramics. One of the primary obstacles in this characterization is the limitation of in-situ transmission electron microscopy (TEM) investigations. Such studies are typically unfeasible due to the high sintering temperatures required for these ceramics, which exceed the operational limits of most TEM setups.

It is hence desirable to employ theoretical models and numerical simulations to evaluate SCLs and abnormal grain growth. De Souza derived numerical solutions based on defect chemistry in acceptor-doped oxide systems at equilibrium state [30]. The impacts of different charge species, the formation energy difference of oxygen vacancy and dopant between GB core and bulk phase, temperature and partial pressure of oxygen on grain boundary potential are comprehensively studied in a bicrystal with planar GB core. However, applying these numerical solutions to polycrystalline cases is impractical. Under this circumstance, the phase-field method with a diffuse interface emerges as a powerful tool to solve different moving boundary problems [31, 32]. There are a series of phase-field sintering models, e.g. to consider the solute drag effect in metals [24] and ceramics [33] and for non-isothermal sintering [34–37]. But these models do not consider the charged defects, electrostatics or defect chemistry, which are important for oxide ceramics. Recently, Vikrant et al. developed a multi-physics phase-field model with an emphasis on GB misorientation and investigate the SCL formation at equilibrium and quasi-equilibrium state [38]. Then, this model is applied to explain the abnormal grain growth with a bimodal pattern as observed in experiments [39]. However, in this phase-field model the defect chemistry is not explicitly included, and thus there is no simulation results dedicated to the influence of defect energetics on SCLs and abnormal grain growth.

In the present work, we develop a phase-field grain growth model founded on the principle of defect-chemistry to simulate SCL formation and abnormal grain growth during sintering of oxide electroceramics. By taking into account the formation energy differences and the equilibrium defect concentrations in bulk and GB core, the thermodynamic descriptions of point defects are included in the phase-field model, along with the kinetics of grain boundary motion and defect diffusion. The spatio-temporal distributions of defect concentration and electrostatic potential in the grain interior and at GB are then solved self-consistently.

The outline of this paper is as follows. Section 2 presents the fundamentals of defect chemistry and the classical sharp interface bicrystal models, i.e., the GC and MS models, for they serve as important benchmarks in later sections. Section 3 describes the grain growth phase-field model in the principle of defect chemistry and electrostatics. Then, we demonstrate the implementation of the phase-field model via the finite element method in Section 4. The capabilities of this model are discussed for bicrystal and polycrystalline cases in Section 5. Thereby the solute drag induced abnormal grain growth simulation results are systematically presented and discussed, particularly in terms of the impact of segregation energies. It is followed by a concluding Section 6.

## 2. Defect chemistry of oxide ceramics

The basics of defect chemistry and the sharp interface bicrystal models (the MS and the GC models) for the equilibrium state were well described in Refs. [16, 30, 40]. Thereby the GB is treated as sharp interface with GB core properties. Thus the concentration profiles of oxygen

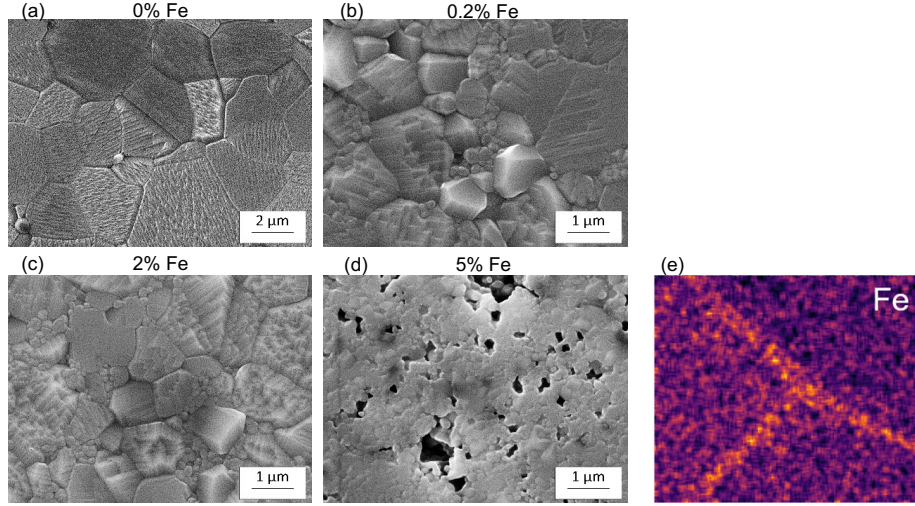


Figure 1: Microstructures in undoped (a) and Fe-doped STO (b-d) after heating to 1300°C for 10h. With increasing Fe concentration, less grain growth occurs. A fraction of very small grains appears in the microstructures for 0.2% Fe. For 2% Fe, (c), more such small grains are evident, until for 5% Fe, all grains remain small. Note the different scale in (a) [25]. (e) Fe segregation to the grain boundaries as evident by STEM-EDS [26]. Sources: 10.1016/j.jeurceramsoc.2022.11.074, 10.1016/j.actamat.2024.119941

vacancy and dopant are discontinuous, with concentration jumps across the GB core. For the bicrystal, it becomes a one-dimensional case.

Assume a coordinate system  $x$ , with the origin  $x = 0$  located at the GB core. Moreover, point defects are assumed to be dilute and non-interacting in both GB core and bulk phases. Therefore, the electrochemical potentials of oxygen vacancy and dopant in the bulk and in the core region can be formulated [30] as

$$\mu_{V_{\ddot{O}},b}(x) = \mu_{V_{\ddot{O}},b}^0 + k_B T \ln \left[ \frac{c_{V_{\ddot{O}},b}(x)}{N_{V_{\ddot{O}},b} - c_{V_{\ddot{O}},b}(x)} \right] + z_{V_{\ddot{O}}} e \phi(x), \quad (1)$$

$$\mu_{dop,b}(x) = \mu_{dop,b}^0 + k_B T \ln \left[ \frac{c_{dop,b}(x)}{N_{dop,b} - c_{dop,b}(x)} \right] + z_{dop} e \phi(x), \quad (2)$$

$$\mu_{V_{\ddot{O}},c} = \mu_{V_{\ddot{O}},c}^0 + k_B T \ln \left[ \frac{c_{V_{\ddot{O}},c}}{N_{V_{\ddot{O}},c} - c_{V_{\ddot{O}},c}} \right] + z_{V_{\ddot{O}}} e \Phi_0, \quad (3)$$

$$\mu_{dop,c} = \mu_{dop,c}^0 + k_B T \ln \left[ \frac{c_{dop,c}}{N_{dop,c} - c_{dop,c}} \right] + z_{dop} e \Phi_0, \quad (4)$$

where  $\mu_{V_{\ddot{O}},b}^0$ ,  $\mu_{V_{\ddot{O}},c}^0$ ,  $\mu_{dop,b}^0$  and  $\mu_{dop,c}^0$  denote the standard formation energies of oxygen vacancy and dopant in the bulk and in the core, respectively. The symbols  $N_{V_{\ddot{O}},b}^0$ ,  $N_{V_{\ddot{O}},c}^0$ ,  $N_{dop,b}^0$  and  $N_{dop,c}^0$  indicate the number of available sites per unit volume of oxygen vacancy and dopant in the bulk and core, respectively.  $z_{V_{\ddot{O}}}$  and  $z_{dop}$  denote the charge numbers of oxygen vacancy and acceptor dopant.  $\phi(x)$  is the electrostatic potential, and  $\Phi_0$  is the electrostatic potential in the GB core. Similarly,  $c_{dop,c}$  and  $c_{V_{\ddot{O}},c}$  are the concentrations of dopant and oxygen vacancy in the GB core.

Thus, we have  $\Phi_0 = \phi(0)$ ,  $c_{\text{dop},c} = c_{\text{dop},b}(0)$  and  $c_{V_{\ddot{O}},c} = c_{V_{\ddot{O}},b}(0)$ . Additionally,  $k_B$ ,  $e$  and  $T$  are the Boltzmann constant, elementary charge and temperature, respectively. The formation of a SCL requires the segregation of oxygen vacancy in the core. The smaller value of  $\mu_{V_{\ddot{O}},c}^0$  than  $\mu_{V_{\ddot{O}},b}^0$ , i.e.  $\mu_{V_{\ddot{O}},c}^0 - \mu_{V_{\ddot{O}},b}^0 < 0$ , drives the formation of SCL. At the equilibrium state, when electrochemical potentials should be everywhere the same (in other words, no gradient), we have

$$\mu_{V_{\ddot{O}},c} = \mu_{V_{\ddot{O}},b}(x) = \mu_{V_{\ddot{O}},b}(\infty), \quad (5)$$

$$\mu_{\text{dop},c} = \mu_{\text{dop},b}(x) = \mu_{\text{dop},b}(\infty), \quad (6)$$

Hence, equilibrium concentration profiles of oxygen vacancy and dopant in the SCL take the form

$$c_{V_{\ddot{O}},b}(x) = c_{V_{\ddot{O}},b}(\infty) \exp \left[ \frac{-z_{V_{\ddot{O}}} e \{ \phi(x) - \phi(\infty) \}}{k_B T} \right], \quad (7)$$

$$c_{\text{dop},b}(x) = \frac{c_{\text{dop},b}(\infty) N_{\text{dop},b} \exp \left[ \frac{-z_{\text{dop}} e \{ \phi(x) - \phi(\infty) \}}{k_B T} \right]}{N_{\text{dop},b} + c_{\text{dop},b}(\infty) \left\{ \exp \left[ \frac{-z_{\text{dop}} e \{ \phi(x) - \phi(\infty) \}}{k_B T} \right] - 1 \right\}}. \quad (8)$$

In analogy, equilibrium concentrations of oxygen vacancy and dopant in the core are

$$c_{V_{\ddot{O}},c} = \frac{N_{V_{\ddot{O}},c} c_{V_{\ddot{O}},b}(\infty) \exp \left[ -\frac{\Delta g_{V_{\ddot{O}}} + z_{V_{\ddot{O}}} e \Phi_0}{k_B T} \right]}{N_{V_{\ddot{O}},b} + c_{V_{\ddot{O}},b}(\infty) \exp \left[ -\frac{\Delta g_{V_{\ddot{O}}} + z_{V_{\ddot{O}}} e \Phi_0}{k_B T} \right]}, \quad (9)$$

$$c_{\text{dop},c} = \frac{N_{\text{dop},c} c_{\text{dop},b}(\infty) \exp \left[ -\frac{\Delta g_{\text{dop}} + z_{\text{dop}} e \Phi_0}{k_B T} \right]}{N_{\text{dop},b} + c_{\text{dop},b}(\infty) \exp \left[ -\frac{\Delta g_{\text{dop}} + z_{\text{dop}} e \Phi_0}{k_B T} \right]}, \quad (10)$$

where  $\Delta g_{V_{\ddot{O}}} = \mu_{V_{\ddot{O}},c}^0 - \mu_{V_{\ddot{O}},b}^0$  and  $\Delta g_{\text{dop}} = \mu_{\text{dop},c}^0 - \mu_{\text{dop},b}^0$ . All parameters are tabulated in Table 1.

### 2.1. The Mott-Schottky model

The Mott-Schottky model assumes that the dopant is immobile and its concentration remains fixed and constant everywhere, i.e.  $\nabla c_{\text{dop}} = 0$ . Note that this assumption simplifies the scenario but breaks the equilibrium condition of the electrochemical potential of the dopants. Based on the assumption, Poisson's equation can be written as

$$\begin{aligned} \epsilon_0 \epsilon_r \frac{\partial^2 \phi}{\partial x^2} &= -\rho(x) \\ &= -e [z_{\text{dop}} c_{\text{dop},b}(\infty) + z_{V_{\ddot{O}}} c_{V_{\ddot{O}},b}(x)]. \end{aligned} \quad (11)$$

Substituting  $c_{\text{dop},b}(\infty) = 2c_{V_{\ddot{O}},b}(\infty)$  into Eq. (11), we have

$$\epsilon_0 \epsilon_r \frac{\partial^2 \phi}{\partial x^2} = 2e c_{V_{\ddot{O}},b}(\infty) \left\{ 1 - \exp \left[ \frac{-2e \{ \phi(x) - \phi(\infty) \}}{k_B T} \right] \right\}. \quad (12)$$

With  $l_D = \sqrt{\frac{\epsilon_0 \epsilon_r k_B T}{2e^2 c_{\text{dop},b}(\infty)}}$  being the Debye length and  $\alpha = \frac{e}{k_B T}$ , Eq.(12) becomes

$$\frac{\partial^2 \phi}{\partial x^2} = \frac{1}{2\alpha l_D^2} \left\{ 1 - \exp \left[ \frac{-2e \{ \phi(x) - \phi(\infty) \}}{k_B T} \right] \right\}, \quad (13)$$

Table 1: Summary of the parameters in the sharp interface method

Parameter	Definition	Unit
$\mu_{V_{\ddot{O}},b}^0$	Formation energy of oxygen vacancy in the bulk phase	eV
$\mu_{V_{\ddot{O}},c}^0$	Formation energy of oxygen vacancy in the core region	eV
$\mu_{dop,b}^0$	Formation energy of dopant in the bulk phase	eV
$\mu_{dop,c}^0$	Formation energy of dopant in the core region	eV
$\Delta g_{V_{\ddot{O}}}$	The difference of formation energy of oxygen vacancy between core and bulk, i.e. $\Delta g_{V_{\ddot{O}}} = \mu_{V_{\ddot{O}},c}^0 - \mu_{V_{\ddot{O}},b}^0$	eV
$\Delta g_{dop}$	The difference of formation energy of dopant between core and bulk, i.e. $\Delta g_{dop} = \mu_{dop,c}^0 - \mu_{dop,b}^0$	eV
$N_{V_{\ddot{O}},b}$	Maximum number density of oxygen vacancy in the bulk phase	$\frac{1}{m^3}$
$N_{V_{\ddot{O}},c}$	Maximum number density of oxygen vacancy in the core region	$\frac{1}{m^3}$
$N_{dop,b}$	Maximum number density of dopant in the bulk phase. $N_{dop,b} = 1/a^3$ , with $a$ being the perovskite lattice constant	$\frac{1}{m^3}$
$N_{dop,c}$	Maximum number density of dopant in the core region	$\frac{1}{m^3}$
$z_{V_{\ddot{O}}}$	Valency number of oxygen vacancy, $z_{V_{\ddot{O}}} = 2$	-
$z_{dop}$	Valency number of dopant, $z_{dop} = -1$ for $Fe_{Ti}$ in Fe-doped STO	-
$c_{dop,b}(\infty)$	Number density of dopant in the bulk far from the core region	$\frac{1}{m^3}$
$c_{V_{\ddot{O}},b}(\infty)$	Number density of oxygen vacancy in the bulk far from the core region	$\frac{1}{m^3}$
$k_B$	Boltzmann constant $k_B = 1.38 \times 10^{-23}$	$\frac{J}{K}$
$T$	Temperature	K
$\epsilon_0$	Vacuum permittivity $\epsilon_0 = 8.854 \times 10^{-12}$	$\frac{C}{Vm}$
$\epsilon_r$	Relative permittivity	-
$w_c$	width of the core	m

## 2.2. The Gouy-Chapman model

In the Gouy-Chapman model both point defects (oxygen vacancies and dopant) are mobile. The electrochemical potential of the acceptor dopant is also considered to be constant, as is that of the oxygen vacancies. Thus, Poisson's equation becomes

$$\begin{aligned} \epsilon_0 \epsilon_r \frac{\partial^2 \phi}{\partial x^2} &= -\rho(x) \\ &= -e[z_{dop} c_{dop,b}(x) + z_{V_{\ddot{O}}} c_{V_{\ddot{O}},b}(x)]. \end{aligned} \quad (14)$$

Substituting Eq. (7) and (8) into (14), we have

$$\begin{aligned} \epsilon_0 \epsilon_r \frac{\partial^2 \phi}{\partial x^2} &= -e \left\{ z_{dop} \frac{c_{dop,b}(\infty) N_{dop,b} \exp \left[ \frac{-z_{dop} e \{ \phi(x) - \phi(\infty) \}}{k_B T} \right]}{N_{dop,b} + c_{dop,b}(\infty) \left\{ \exp \left[ \frac{-z_{dop} e \{ \phi(x) - \phi(\infty) \}}{k_B T} \right] - 1 \right\}} \right. \\ &\quad \left. + z_{V_{\ddot{O}}} c_{V_{\ddot{O}},b}(\infty) \exp \left[ \frac{-z_{V_{\ddot{O}}} e \{ \phi(x) - \phi(\infty) \}}{k_B T} \right] \right\}. \end{aligned} \quad (15)$$

The numerical solutions of the MS and GC models have been achieved through an iteration process [30]. In the present work, we propose an alternative numerical method via finite element

method (FEM). By considering the symmetric configuration of a bicrystal (ignoring the grain mis-orientation), the semi-infinite simulation domain of  $[0, \infty)$  is sufficient. The location of the GB core is located at the left boundary of the semi-infinite domain ( $x = 0$ ). As for the boundary conditions, the electrostatic field is grounded at the right side, i.e.,  $\phi|_{x=\infty} = 0$ , while at the left side, a mixed boundary condition is given by

$$\left. \frac{\partial \phi}{\partial x} \right|_{x=0} = -\frac{Q_c(\phi_0)}{2\epsilon_0\epsilon_r}, \quad (16)$$

where  $Q_c(\phi_0) = ew_c(z_{V_{\odot}}c_{V_{\odot},c} + z_{\text{dop}}c_{\text{dop},c})$  and  $\phi_0 = \phi|_{x=0}$ . We employed the boundary element in the finite element method to regard directly the mixed type of boundary condition defined in the above equation. The obtained numerical solutions agree fully with these from Ref. [30] (See Supplementary).

### 3. Phase-field grain growth model with defect chemistry and electrostatics

#### 3.1. Free energy density functional and electrochemical potentials

We include here the defect chemistry into the grain growth model for oxide ceramics, with Fe-doped STO as a prototype. Upon grain contact in Fe-doped STO, the lower formation energy of oxygen vacancy in the core compels point defects to segregate towards the GB core. Afterwards, the depletion or accumulation zone appears in the vicinity of GB core. The SCL forms through a diffusion process. The handling of SCL is similarly addressed in Ref. [30]. The segregation of point defects in the core serves to dissipate the total free energy of the system and also induces solute drag effect when the core moves.

Assuming an Fe-doped STO polycrystalline system consisting of  $n$  grains, we choose Kim-Kim-Suzuki (KKS) phase-field model and utilize a set of non-conserved order parameters (OPs)  $\eta_i$  to distinguish between different grains [41]. Within grain  $i$ ,  $\eta_i = 1$  and  $\eta_j = 0$  for  $j < n$  and  $j \neq i$ . Within the core region of grain  $i$  and  $j$ , the order parameters  $\eta_i$  and  $\eta_j$  spatially vary from 0 to 1. In the latter context,  $\eta$  denotes the entire set of OPs  $\{\eta_i\}$ . When considering electrochemical contributions, we employ two conserved concentration fields along with an electrostatic potential field. Other normalized field variables are  $C_{V_{\odot}}$  for oxygen vacancy concentration,  $C_{\text{dop}}$  for dopant concentration, and  $\phi$  for the electrostatic potential. In Fe-doped STO,  $\text{Fe}^{3+}$  and  $\text{Fe}^{4+}$  can coexist. At high temperatures and low oxygen partial pressures, a higher proportion of  $\text{Fe}^{3+}$  is observed and thus the dopant  $\text{Fe}'_{\text{Ti}}$  has negative charge. For example, during the sintering process at 1623 K in air, approximately 90% of the iron is estimated to be in the  $\text{Fe}^{3+}$  state, according to the bulk defect chemical model (see Fig. A1 in Ref. [42]). Thus, in this study, we assume the valence state of Fe to be 3+ and therefore the valence of dopant  $\text{Fe}'_{\text{Ti}}$  is -1, i.e.  $z_{\text{dop}} = -1$ . Then, the formulation of total free energy density functional is given by

$$\mathcal{F} = \int_{\Omega} (f^{\text{grad}} + f^{\text{loc}} + f^{\text{ech}}) d\Omega. \quad (17)$$

$f^{\text{grad}}$  represents the gradient term, it is given by

$$f^{\text{grad}} = \frac{1}{2}\kappa \sum_{i=1}^n |\nabla \eta_i|^2, \quad (18)$$

where  $\kappa$  is the coefficient of the gradient term.  $f^{\text{loc}}$  is the well potential. According to Ref. [43], its formulation is given by

$$f^{\text{loc}} = \omega \sum_{i=1}^n \left( \frac{\eta_i^4}{4} - \frac{\eta_i^2}{2} + \gamma \sum_{i=1}^n \sum_{j>i}^n \eta_i^2 \eta_j^2 + \frac{1}{4} \right), \quad (19)$$

with  $\gamma = 1.5$  for producing symmetric profile of  $\eta$  and isotropic grain growth.

The determination of parameters such as  $\kappa$  and  $\omega$  can be linked to characteristics such as core width ( $w_c$ ) and interface energy ( $\sigma$ ). Their relations can be expressed as

$$\sigma = \frac{\sqrt{2}}{3} \sqrt{\kappa \omega}, \quad (20)$$

and

$$w_c = \sqrt{\frac{8\kappa}{\omega}}. \quad (21)$$

In the present work, we only consider the isotropic interface energy, i.e. it is not dependent on GB misorientation. The third term in free energy functional is the electrochemical contribution. Here, we treat the electrochemical free energy density as a mixture of bulk phase and core by an interpolation function. Thus,  $f^{\text{ech}}$  is

$$f^{\text{ech}} = [1 - h(\eta)] f_b^{\text{ech}}(C_{\text{V}\ddot{\text{O}},\text{b}}, C_{\text{dop},\text{b}}) + h(\eta) f_c^{\text{ech}}(C_{\text{V}\ddot{\text{O}},\text{c}}, C_{\text{dop},\text{c}}) - \frac{\epsilon_0 \epsilon_r}{2} (\nabla \phi)^2, \quad (22)$$

where the subscripts b and c indicate the bulk phase and core, respectively.  $h(\eta)$  is the interpolation function and is given by

$$h(\eta) = \frac{4}{3} \left[ 1 - 4 \sum_{i=1}^n \eta_i^3 + 3 \left( \sum_{i=1}^n \eta_i^2 \right)^2 \right]. \quad (23)$$

Here,  $h(\eta)$  exhibits non-monotonic behavior. Specifically, for an  $i/j$  GB,  $h(\eta_i) = 0$  when  $\eta_i = 1$  (representing the bulk phase), whereas  $h(\eta_i) = 1$  when  $\eta_i = 0.5$  (representing the core). This interpolation function allows us to differentiate between the bulk phase and the core region.  $\epsilon_0$  is the vacuum permittivity;  $\epsilon_r$  is the relative permittivity. For STO,  $\epsilon_r = 9 \times 10^4 / (T - 35)$  [30].  $\epsilon_r$  is only dependent on temperature in the present work. Hence,  $\epsilon_r$  is constant across the SCL zone for specific temperature. Furthermore,  $f_b^{\text{ech}}(C_{\text{V}\ddot{\text{O}},\text{b}}, C_{\text{dop},\text{b}})$  and  $f_c^{\text{ech}}(C_{\text{V}\ddot{\text{O}},\text{c}}, C_{\text{dop},\text{c}})$  in Eq. (22) denote the electrochemical free energy contributions from the bulk and core, respectively, with  $C_{\text{V}\ddot{\text{O}},\text{b}}$  and  $C_{\text{dop},\text{b}}$  being the phase concentrations of oxygen vacancy and dopant in the bulk phase, while  $C_{\text{V}\ddot{\text{O}},\text{c}}$  and  $C_{\text{dop},\text{c}}$  being the phase concentrations of oxygen vacancy and dopant in the core. When  $h(\eta) = 1$ ,  $C_{\text{dop},\text{c}}$  and  $C_{\text{V}\ddot{\text{O}},\text{c}}$  correspond to  $c_{\text{dop},\text{c}}$  and  $c_{\text{V}\ddot{\text{O}},\text{c}}$ . When  $h(\eta) = 0$ ,  $C_{\text{dop},\text{b}}$  and  $C_{\text{V}\ddot{\text{O}},\text{b}}$  are same as  $c_{\text{dop},\text{b}}(x)$  and  $c_{\text{V}\ddot{\text{O}},\text{b}}(x)$ . Local concentration is treated as the mixture of phase concentrations in bulk and core. The relations between local concentration and phase concentration are expressed as

$$C_{\text{V}\ddot{\text{O}}} = [1 - h(\eta)] C_{\text{V}\ddot{\text{O}},\text{b}} + h(\eta) C_{\text{V}\ddot{\text{O}},\text{c}}, \quad (24)$$

$$C_{\text{dop}} = [1 - h(\eta)] C_{\text{dop},\text{b}} + h(\eta) C_{\text{dop},\text{c}}. \quad (25)$$

In principle of the thermodynamic model extended by Ref. [30], the expressions for the electrochemical free energies  $f_c^{\text{ech}}(C_{V_{\ddot{O}},c}, C_{\text{dop},c})$  and  $f_b^{\text{ech}}(C_{V_{\ddot{O}},b}, C_{\text{dop},b})$  are given by

$$\begin{aligned} f_c^{\text{ech}}(C_{V_{\ddot{O}},c}, C_{\text{dop},c}) = & \frac{1}{V_m} \left\{ g_{V_{\ddot{O}},c}^0 C_{V_{\ddot{O}},c} + g_{\text{dop},c}^0 C_{\text{dop},c} \right. \\ & + RT \left[ C_{V_{\ddot{O}},c} \ln(C_{V_{\ddot{O}},c}) + (\tilde{N}_{V_{\ddot{O}},c} - C_{V_{\ddot{O}},c}) \ln(\tilde{N}_{V_{\ddot{O}},c} - C_{V_{\ddot{O}},c}) \right. \\ & \left. \left. + C_{\text{dop},c} \ln(C_{\text{dop},c}) + (\tilde{N}_{\text{dop},c} - C_{\text{dop},c}) \ln(\tilde{N}_{\text{dop},c} - C_{\text{dop},c}) \right] \right\} \\ & + \frac{\mathcal{F}}{V_m} (z_{V_{\ddot{O}}} C_{V_{\ddot{O}},c} + z_{\text{dop}} C_{\text{dop},c}) \phi, \end{aligned} \quad (26)$$

$$\begin{aligned} f_b^{\text{ech}}(C_{V_{\ddot{O}},b}, C_{\text{dop},b}) = & \frac{1}{V_m} \left\{ g_{V_{\ddot{O}},b}^0 C_{V_{\ddot{O}},b} + g_{\text{dop},b}^0 C_{\text{dop},b} \right. \\ & + RT \left[ C_{V_{\ddot{O}},b} \ln(C_{V_{\ddot{O}},b}) + (\tilde{N}_{V_{\ddot{O}},b} - C_{V_{\ddot{O}},b}) \ln(\tilde{N}_{V_{\ddot{O}},b} - C_{V_{\ddot{O}},b}) \right. \\ & \left. \left. + C_{\text{dop},b} \ln(C_{\text{dop},b}) + (\tilde{N}_{\text{dop},b} - C_{\text{dop},b}) \ln(\tilde{N}_{\text{dop},b} - C_{\text{dop},b}) \right] \right\} \\ & + \frac{\mathcal{F}}{V_m} (z_{V_{\ddot{O}}} C_{V_{\ddot{O}},b} + z_{\text{dop}} C_{\text{dop},b}) \phi, \end{aligned} \quad (27)$$

where  $g_{V_{\ddot{O}},c}^0$ ,  $g_{V_{\ddot{O}},b}^0$ ,  $g_{\text{dop},c}^0$ ,  $g_{\text{dop},b}^0$  are standard formation energies of oxygen vacancy and dopant in bulk and core.  $\tilde{N}_{V_{\ddot{O}},c}$ ,  $\tilde{N}_{V_{\ddot{O}},b}$ ,  $\tilde{N}_{\text{dop},c}$ ,  $\tilde{N}_{\text{dop},b}$  are dimensionless numbers of available sites per unit volume for oxygen vacancy and dopant in bulk and core.  $z_{V_{\ddot{O}}}$  and  $z_{\text{dop}}$  are valance numbers of oxygen vacancy and dopant.  $\mathcal{F}$ ,  $V_m$ ,  $R$ ,  $T$  are the Faraday constant, molar volume, gas constant and temperature, respectively. The electrochemical potentials of oxygen vacancy and dopant in bulk and core are obtained by

$$\mu_{V_{\ddot{O}},b}^{\text{PF}} = \frac{\delta \mathcal{F}}{\delta C_{V_{\ddot{O}},b}} = \frac{g_{V_{\ddot{O}},b}^0}{V_m} + \frac{RT}{V_m} \ln \left[ \frac{C_{V_{\ddot{O}},b}}{\tilde{N}_{V_{\ddot{O}},b} - C_{V_{\ddot{O}},b}} \right] + \frac{\mathcal{F}}{V_m} z_{V_{\ddot{O}}} \phi, \quad (28)$$

$$\mu_{V_{\ddot{O}},c}^{\text{PF}} = \frac{\delta \mathcal{F}}{\delta C_{V_{\ddot{O}},c}} = \frac{g_{V_{\ddot{O}},c}^0}{V_m} + \frac{RT}{V_m} \ln \left[ \frac{C_{V_{\ddot{O}},c}}{\tilde{N}_{V_{\ddot{O}},c} - C_{V_{\ddot{O}},c}} \right] + \frac{\mathcal{F}}{V_m} z_{V_{\ddot{O}}} \phi, \quad (29)$$

$$\mu_{\text{dop},b}^{\text{PF}} = \frac{\delta \mathcal{F}}{\delta C_{\text{dop},b}} = \frac{g_{\text{dop},b}^0}{V_m} + \frac{RT}{V_m} \ln \left[ \frac{C_{\text{dop},b}}{\tilde{N}_{\text{dop},b} - C_{\text{dop},b}} \right] + \frac{\mathcal{F}}{V_m} z_{\text{dop}} \phi, \quad (30)$$

$$\mu_{\text{dop},c}^{\text{PF}} = \frac{\delta \mathcal{F}}{\delta C_{\text{dop},c}} = \frac{g_{\text{dop},c}^0}{V_m} + \frac{RT}{V_m} \ln \left[ \frac{C_{\text{dop},c}}{\tilde{N}_{\text{dop},c} - C_{\text{dop},c}} \right] + \frac{\mathcal{F}}{V_m} z_{\text{dop}} \phi, \quad (31)$$

which are consistent with the standard formations of electrochemical potentials in defect chemistry, i.e. Eq. (1) to Eq. (4).

### 3.2. Governing equations

In the framework of KKS phase-field model, the evolution of phase-field OPs obeys the Allen-Cahn equation. For grain  $i$ , the evolution of  $\eta_i$  in time is

$$\frac{1}{L} \frac{\partial \eta_i}{\partial t} = \frac{\delta \mathcal{F}}{\delta \eta_i}, \quad (32)$$



where  $L$  is the GB mobility. Substituting Eq. (17) into (32), we can obtain

$$\begin{aligned} \frac{1}{L} \frac{\partial \eta_i}{\partial t} &= \nabla \cdot \kappa \nabla \eta_i - \omega \frac{\partial f^{\text{loc}}(\eta)}{\partial \eta_i} \\ &+ \frac{\partial h(\eta)}{\partial \eta_i} \left[ f_b^{\text{ech}} - f_c^{\text{ech}} - \frac{\partial f_b^{\text{ech}}}{\partial C_{V_{\ddot{O}},b}} (C_{V_{\ddot{O}},b} - C_{V_{\ddot{O}},c}) - \frac{\partial f_b^{\text{ech}}}{\partial C_{\text{dop},b}} (C_{\text{dop},b} - C_{\text{dop},c}) \right]. \end{aligned} \quad (33)$$

At the quasi-equilibrium state, the core moves with a constant velocity,  $v_c$ , we have  $\dot{\eta} = -v_c \eta'(x)$ , thus Eq. (32) becomes

$$\begin{aligned} \frac{v_c}{L} \frac{d\eta}{dx} &= \nabla \cdot \kappa \nabla \eta_i - \omega \frac{\partial f^{\text{loc}}(\eta)}{\partial \eta_i} \\ &+ \frac{\partial h(\eta)}{\partial \eta_i} \left[ f_b^{\text{ech}} - f_c^{\text{ech}} - \frac{\partial f_b^{\text{ech}}}{\partial C_{V_{\ddot{O}},b}} (C_{V_{\ddot{O}},b} - C_{V_{\ddot{O}},c}) - \frac{\partial f_b^{\text{ech}}}{\partial C_{\text{dop},b}} (C_{\text{dop},b} - C_{\text{dop},c}) \right], \end{aligned} \quad (34)$$

Conserved concentration fields  $C_{V_{\ddot{O}}}$  and  $C_{\text{dop}}$  follow Fick's law, which are expressed as

$$\frac{\partial C_{V_{\ddot{O}}}}{\partial t} = \nabla \cdot \left( M_{V_{\ddot{O}}} \nabla \frac{\delta \mathcal{F}}{\delta C_{V_{\ddot{O}}}} \right), \quad (35)$$

$$\frac{\partial C_{\text{dop}}}{\partial t} = \nabla \cdot \left( M_{\text{dop}} \nabla \frac{\delta \mathcal{F}}{\delta C_{\text{dop}}} \right), \quad (36)$$

where  $M_{V_{\ddot{O}}}$  and  $M_{\text{dop}}$  are mobilities of oxygen vacancy and dopant, which are given by  $M_{V_{\ddot{O}}} = \frac{D_{V_{\ddot{O}}}}{\partial^2 f^{\text{ech}} / \partial C_{V_{\ddot{O}}}^2}$  and  $M_{\text{dop}} = \frac{D_{\text{dop}}}{\partial^2 f^{\text{ech}} / \partial C_{\text{dop}}^2}$ , with  $D_{V_{\ddot{O}}}$  and  $D_{\text{dop}}$  being the diffusivities of oxygen vacancy and dopant, respectively. Moreover, local equilibrium between bulk phases and core should be satisfied everywhere. Therefore, we have following constrains

$$\delta \mathcal{F} / \delta C_{V_{\ddot{O}}} = \delta \mathcal{F} / \delta C_{V_{\ddot{O}},b} = \delta \mathcal{F} / \delta C_{\text{dop},b}, \quad (37)$$

$$\delta \mathcal{F} / \delta C_{\text{dop}} = \delta \mathcal{F} / \delta C_{V_{\ddot{O}},c} = \delta \mathcal{F} / \delta C_{\text{dop},c}. \quad (38)$$

Therefore,  $\delta \mathcal{F} / \delta C_{V_{\ddot{O}}}$  and  $\delta \mathcal{F} / \delta C_{\text{dop}}$  in Eqs. (35) and (36) can be substituted by  $\mu_{V_{\ddot{O}},b}^{\text{PF}}$ ,  $\mu_{\text{dop},b}^{\text{PF}}$  or  $\mu_{V_{\ddot{O}},c}^{\text{PF}}$ ,  $\mu_{\text{dop},c}^{\text{PF}}$ . In addition, the governing equation of electrostatic potential field is obtained by Poisson's equation

$$\epsilon_0 \epsilon_r \nabla^2 \phi + \frac{\mathcal{F}}{V_m} (z_{V_{\ddot{O}}} C_{V_{\ddot{O}}} + z_{\text{dop}} C_{\text{dop}}) = 0, \quad (39)$$

The parameters utilized in phase-field model are tabulated in table 2.

#### 4. Finite element implementation of the phase-field model

In this section, we present the detailed finite element implementation for the defect-chemistry informed phase-field model. According to the model presented in Section 3 and Table 2, we treat the OPs  $\eta_i$  and the field variables  $C_{V_{\ddot{O}}}$ ,  $C_{\text{dop}}$ ,  $C_{V_{\ddot{O}},b}$ ,  $C_{V_{\ddot{O}},c}$ ,  $C_{\text{dop},b}$ ,  $C_{\text{dop},c}$ ,  $\phi$  as degrees-of-freedom (DOFs). Moreover, to solve Eqs. (35) and (36), we use the mixed finite element formulation and treat the electro-chemical potentials  $\mu_{V_{\ddot{O}}}$  and  $\mu_{\text{dop}}$  as additional DOFs [44].

Table 2: Summary of the parameters in the phase-field model

DOFs	Definition	Unit
$\eta_i$	phase-field order parameter of grain $i$ , $i = 1, 2, 3, \dots, n$	-
$C_{V\ddot{o}}$	Normalized local concentration of oxygen vacancy ( $C_{V\ddot{o}} = a^3 c_{V\ddot{o}}$ , with $a$ being the lattice constant)	-
$C_{\text{dop}}$	Normalized local concentration of dopant, $C_{\text{dop}} = a^3 c_{\text{dop}}$	-
$C_{V\ddot{o},b}$	Normalized concentration of oxygen vacancy in bulk phase, $C_{V\ddot{o},b} = a^3 c_{V\ddot{o},b}$	-
$C_{V\ddot{o},c}$	Normalized concentration of oxygen vacancy in core region, $C_{V\ddot{o},c} = a^3 c_{V\ddot{o},c}$	-
$C_{\text{dop},b}$	Normalized concentration of dopant in bulk phase, $C_{\text{dop},b} = a^3 c_{\text{dop},b}$	-
$C_{\text{dop},c}$	Normalized concentration of dopant in core region, $C_{\text{dop},c} = a^3 c_{\text{dop},c}$	-
$\phi$	Electrostatic potential	V
Parameters	Definition	Unit
$\kappa$	Coefficient of gradient term	$\frac{\text{J}}{\text{m}}$
$\omega$	Heigh of well potential	$\frac{\text{J}}{\text{m}^3}$
$L$	GB mobility	$\frac{\text{m}^3}{\text{Js}}$
$g_{V\ddot{o},b}^0$	Formation energy of oxygen vacancy in the bulk phase. $g_{V\ddot{o},b}^0 = \mu_{V\ddot{o},b}^0 N_A$ , with $N_A$ being Avogadro constant	$\frac{\text{J}}{\text{mol}}$
$g_{V\ddot{o},c}^0$	Formation energy of oxygen vacancy in the core region. $g_{V\ddot{o},c}^0 = \mu_{V\ddot{o},c}^0 N_A$	$\frac{\text{J}}{\text{mol}}$
$g_{\text{dop},b}^0$	Formation energy of dopant in the bulk phase. $g_{\text{dop},b}^0 = \mu_{\text{dop},b}^0 N_A$	$\frac{\text{J}}{\text{mol}}$
$g_{\text{dop},c}^0$	Formation energy of dopant in the core region. $g_{\text{dop},c}^0 = \mu_{\text{dop},c}^0 N_A$	$\frac{\text{J}}{\text{mol}}$
$V_m$	Molar volume	$\frac{\text{m}^3}{\text{mol}}$
$\tilde{N}_{V\ddot{o},c}$	Dimensionless available sites of oxygen vacancy in core region. $\tilde{N}_{V\ddot{o},c} = N_{V\ddot{o},c} a^3$ , with $a$ being the lattice constant	-
$\tilde{N}_{V\ddot{o},b}$	Dimensionless available sites of oxygen vacancy in bulk phase. $\tilde{N}_{V\ddot{o},b} = N_{V\ddot{o},b} a^3$	-
$\tilde{N}_{\text{dop},c}$	Dimensionless available sites of dopant in core region. $\tilde{N}_{\text{dop},c} = N_{\text{dop},c} a^3$	-
$\tilde{N}_{\text{dop},b}$	Dimensionless available sites of dopant in bulk phase. $\tilde{N}_{\text{dop},b} = N_{\text{dop},b} a^3$	-
$R$	Gas constant	$\frac{\text{J}}{\text{K}}$
$T$	Temperature	K
$\mathcal{F}$	Faraday constant	$\frac{\text{C}}{\text{mol}}$
$D_{V\ddot{o}}$	Diffusivity of oxygen vacancy	$\frac{\text{m}^2}{\text{s}}$
$D_{\text{dop}}$	Diffusivity of dopant	$\frac{\text{m}^2}{\text{s}}$

The strong forms of the corresponding governing equations have already been given in Eqs. (24), (25) and (33) to (39). According to the FEM [45], we formulate the residuals from the weak forms of these governing equations by introducing corresponding test functions  $\psi_{C_{V\ddot{o},c}}, \psi_{C_{dop,c}}, \psi_{\eta_i}, \psi_{C_{V\ddot{o}}}, \psi_{C_{dop}}, \psi_{\mu_{V\ddot{o}}}, \psi_{\mu_{dop}}, \psi_{C_{V\ddot{o},b}}, \psi_{C_{dop,b}}$  and  $\psi_\phi$ . Firstly, the residuals for the weak forms of Eqs. (24), (25) and (33) are

$$R_{C_{V\ddot{o},c}} = \int_V \psi_{C_{V\ddot{o},c}} \{C_{V\ddot{o}} - [1 - h(\eta)]C_{V\ddot{o},b} - h(\eta)C_{V\ddot{o},c}\} dV, \quad (40)$$

$$R_{C_{dop,c}} = \int_V \psi_{C_{dop,c}} \{C_{dop} - [1 - h(\eta)]C_{dop,b} - h(\eta)C_{dop,c}\} dV, \quad (41)$$

$$\begin{aligned} R_{\eta_i} = & \int_V \psi_{\eta_i} \frac{\eta_i^{t_{n+1}} - \eta_i^{t_n}}{\Delta t} dV + L \int_V \psi_{\eta_i} \omega \frac{\partial f^{\text{loc}}(\eta)}{\partial \eta_i} dV + L \int_V \kappa \eta_{i,j} \psi_{\eta_{i,j}} dV - L \int_\Gamma \kappa \eta_{i,j} \psi_{\eta_i} \hat{n}_j d\Gamma \\ & - L \int_V \psi_{\eta_i} \frac{\partial h(\eta)}{\partial \eta_i} \left[ f_b^{\text{ech}} - f_c^{\text{ech}} - \frac{\partial f_b^{\text{ech}}}{\partial C_{V\ddot{o},b}} (C_{V\ddot{o},b} - C_{V\ddot{o},c}) - \frac{\partial f_b^{\text{ech}}}{\partial C_{dop,b}} (C_{dop,b} - C_{dop,c}) \right] dV. \end{aligned} \quad (42)$$

Note that we use the backward Euler method for the time integration. In the very last equation,  $\eta_i^{t_n}$  and  $\eta_i^{t_{n+1}}$  indicate  $\eta_i$  at the time step  $t_n$  and  $t_{n+1}$ , respectively. Thereby,  $\Delta t = t_{n+1} - t_n$ , and  $\hat{n}_i$  is the normal vector to the boundary  $\Gamma$  of the subdomain. Then, through introducing the addition coupling fields  $\mu_{V\ddot{o}} = \delta \mathcal{F} / \delta C_{V\ddot{o}}$  and  $\mu_{dop} = \delta \mathcal{F} / \delta C_{dop}$ , we obtain the weak forms of Eqs. (35) and (36) as

$$R_{C_{V\ddot{o}}} = \int_V \psi_{C_{V\ddot{o}}} \left( \mu_{V\ddot{o}} - \frac{\delta \mathcal{F}}{\delta C_{V\ddot{o},b}} \right) dV. \quad (43)$$

$$R_{C_{dop}} = \int_V \psi_{C_{dop}} \left( \mu_{dop} - \frac{\delta \mathcal{F}}{\delta C_{dop,b}} \right) dV. \quad (44)$$

$$R_{\mu_{V\ddot{o}}} = \int_V \psi_{\mu_{V\ddot{o}}} \frac{C_{V\ddot{o}}^{t_{n+1}} - C_{V\ddot{o}}^{t_n}}{\Delta t} dV + \int_V M_{V\ddot{o}} \mu_{V\ddot{o},i} \psi_{\mu_{V\ddot{o},i}} dV - \int_\Gamma M_{V\ddot{o}} \mu_{V\ddot{o},i} \psi_{\mu_{V\ddot{o}}} \hat{n}_i d\Gamma. \quad (45)$$

$$R_{\mu_{dop}} = \int_V \psi_{\mu_{dop}} \frac{C_{dop}^{t_{n+1}} - C_{dop}^{t_n}}{\Delta t} dV + \int_V M_{dop} \mu_{dop,i} \psi_{\mu_{dop,i}} dV - \int_\Gamma M_{dop} \mu_{dop,i} \psi_{\mu_{dop}} \hat{n}_i d\Gamma. \quad (46)$$

The weak forms of the local equilibrium constrain in Eqs. (37) and (38) are

$$R_{C_{V\ddot{o},b}} = \int_V \psi_{C_{V\ddot{o},b}} \left( \frac{\delta \mathcal{F}}{\delta C_{V\ddot{o},b}} - \frac{\delta \mathcal{F}}{\delta C_{V\ddot{o},c}} \right) dV. \quad (47)$$

$$R_{C_{dop,b}} = \int_V \psi_{C_{dop,b}} \left( \frac{\delta \mathcal{F}}{\delta C_{dop,b}} - \frac{\delta \mathcal{F}}{\delta C_{dop,c}} \right) dV. \quad (48)$$

Finally, the weak form of Eq (39) is

$$R_\phi = \int_V \epsilon_0 \epsilon_r \phi_{,i} \psi_{\phi,i} dV - \int_\Gamma \epsilon_0 \epsilon_r \phi_{,i} \psi_\phi \hat{n}_i d\Gamma - \int_V \psi_\phi \frac{\mathcal{F}}{V_m} (z_{V\ddot{o}} C_{V\ddot{o}} + z_{\text{dop}} C_{\text{dop}}) dV. \quad (49)$$

Following the Galerkin approach [46], the test functions are discretized as  $\psi_{C_{V\ddot{o},c}} = N_{C_{V\ddot{o},c}}^I \psi_{C_{V\ddot{o},c}}^I$ ,  $\psi_{C_{\text{dop},c}} = N_{C_{\text{dop},c}}^I \psi_{C_{\text{dop},c}}^I$ ,  $\psi_{\eta_i} = N_{\eta_i}^I \psi_{\eta_i}^I$ ,  $\psi_{C_{V\ddot{o}}} = N_{C_{V\ddot{o}}}^I \psi_{C_{V\ddot{o}}}^I$ ,  $\psi_{C_{\text{dop}}} = N_{C_{\text{dop}}}^I \psi_{C_{\text{dop}}}^I$ ,  $\psi_{\mu_{V\ddot{o}}} = N_{\mu_{V\ddot{o}}}^I \psi_{\mu_{V\ddot{o}}}^I$ ,  $\psi_{\mu_{\text{dop}}} = N_{\mu_{\text{dop}}}^I \psi_{\mu_{\text{dop}}}^I$ ,  $\psi_{C_{V\ddot{o},b}} = N_{C_{V\ddot{o},b}}^I \psi_{C_{V\ddot{o},b}}^I$ ,  $\psi_{C_{\text{dop},b}} = N_{C_{\text{dop},b}}^I \psi_{C_{\text{dop},b}}^I$  and  $\psi_\phi = N_\phi \psi_\phi^I$ , where  $I$  denotes the node index and Einstein summation convention is used.  $\psi_{C_{V\ddot{o},c}}^I$ ,  $\psi_{C_{\text{dop},c}}^I$ ,  $\psi_{\eta_i}^I$ ,  $\psi_{C_{V\ddot{o}}}^I$ ,  $\psi_{C_{\text{dop}}}^I$ ,  $\psi_{\mu_{V\ddot{o}}}^I$ ,  $\psi_{\mu_{\text{dop}}}^I$ ,  $\psi_{C_{V\ddot{o},b}}^I$ ,  $\psi_{C_{\text{dop},b}}^I$  and  $\psi_\phi^I$  are the nodal weights, while  $N_{C_{V\ddot{o},c}}^I$ ,  $N_{C_{\text{dop},c}}^I$ ,  $N_{\eta_i}^I$ ,  $N_{C_{V\ddot{o}}}^I$ ,  $N_{C_{\text{dop}}}^I$ ,  $N_{\mu_{V\ddot{o}}}^I$ ,  $N_{\mu_{\text{dop}}}^I$ ,  $N_{C_{V\ddot{o},b}}^I$ ,  $N_{C_{\text{dop},b}}^I$  and  $N_\phi^I$  are the shape functions for the corresponding variables. Then we can write down the discretized residuals as

$$R_{C_{V\ddot{o},c}}^I = \int_V N_{C_{V\ddot{o},c}}^I \{C_{V\ddot{o}} - [1 - h(\eta)]C_{V\ddot{o},b} - h(\eta)C_{V\ddot{o},c}\} dV \quad (50)$$

$$R_{C_{\text{dop},c}}^I = \int_V N_{C_{\text{dop},c}}^I \{C_{\text{dop}} - [1 - h(\eta)]C_{\text{dop},b} - h(\eta)C_{\text{dop},c}\} dV \quad (51)$$

$$R_{\eta_i}^I = \int_V \frac{N_{\eta_i}^I}{\Delta t} dV + L \int_V N_{\eta_i}^I \omega \frac{\partial f^{\text{loc}}(\eta)}{\partial \eta_i} dV + L \int_V \kappa \eta_{i,j} N_{\eta_{i,j}}^I dV - L \int_\Gamma \kappa \eta_{i,j} N_{\eta_i}^I \hat{n}_j d\Gamma \\ - L \int_V N_{\eta_i}^I \frac{\partial h(\eta)}{\partial \eta_i} \left[ f_b^{\text{ech}} - f_c^{\text{ech}} - \frac{\partial f_b^{\text{ech}}}{\partial C_{V\ddot{o},b}} (C_{V\ddot{o},b} - C_{V\ddot{o},c}) - \frac{\partial f_b^{\text{ech}}}{\partial C_{\text{dop},b}} (C_{\text{dop},b} - C_{\text{dop},c}) \right] dV \quad (52)$$

$$R_{C_{V\ddot{o}}}^I = \int_V N_{C_{V\ddot{o}}}^I \left( \mu_{V\ddot{o}} - \frac{\delta \mathcal{F}}{\delta C_{V\ddot{o},b}} \right) dV \quad (53)$$

$$R_{C_{\text{dop}}}^I = \int_V N_{C_{\text{dop}}}^I \left( \mu_{\text{dop}} - \frac{\delta \mathcal{F}}{\delta C_{\text{dop},b}} \right) dV \quad (54)$$

$$R_{\mu_{V\ddot{o}}}^I = \int_V \frac{N_{\mu_{V\ddot{o}}}^I}{\Delta t} dV + \int_V M_{V\ddot{o}} \mu_{V\ddot{o},i} N_{\mu_{V\ddot{o},i}}^I dV - \int_\Gamma M_{V\ddot{o}} \mu_{V\ddot{o},i} N_{\mu_{V\ddot{o}}}^I \hat{n}_i d\Gamma \quad (55)$$

$$R_{\mu_{\text{dop}}}^I = \int_V \frac{N_{\mu_{\text{dop}}}^I}{\Delta t} dV + \int_V M_{\text{dop}} \mu_{\text{dop},i} N_{\mu_{\text{dop},i}}^I dV - \int_\Gamma M_{\text{dop}} \mu_{\text{dop},i} N_{\mu_{\text{dop}}}^I \hat{n}_i d\Gamma \quad (56)$$

$$R_{C_{V\ddot{o},b}}^I = \int_V N_{C_{V\ddot{o},b}}^I \left( \frac{\delta \mathcal{F}}{\delta C_{V\ddot{o},b}} - \frac{\delta \mathcal{F}}{\delta C_{V\ddot{o},c}} \right) dV \quad (57)$$

$$R_{C_{\text{dop},b}}^I = \int_V N_{C_{\text{dop},b}}^I \left( \frac{\delta \mathcal{F}}{\delta C_{\text{dop},b}} - \frac{\delta \mathcal{F}}{\delta C_{\text{dop},c}} \right) dV \quad (58)$$

$$R_\phi^I = \int_V \epsilon_0 \epsilon_r \phi_{,i} N_{\phi,i}^I dV - \int_\Gamma \epsilon_0 \epsilon_r \phi_{,i} N_\phi^I \hat{n}_i d\Gamma - \int_V N_\phi^I \frac{\mathcal{F}}{V_m} (z_{V\ddot{o}} C_{V\ddot{o}} + z_{\text{dop}} C_{\text{dop}}) dV \quad (59)$$

The linearization of the residuals can be written in the element-level linear formulation, in which the terms in the tangent matrix are calculated by  $K_{\xi,\zeta}^{IJ} = \partial R_\xi^I / \partial \zeta^J$ , where  $\xi, \zeta$  indicates individual DOF. The non-zero terms in the tangent matrix are presented in supplementary. The numerical implementation of the proposed phase-field model is carried out in Multiphysics Object-Oriented Simulation Environment (MOOSE) framework [47, 48].

## 5. Phase-field simulation results of Fe-doped SrTiO<sub>3</sub>

We present first in Section 5.1 one-dimensional phase-field simulation results to demonstrate its capability of reproducing the formation of a SCL at equilibrium state. Subsequently, we investigate the influence of solute drag effects induced by the segregation of point defects in the core on the formation of an asymmetric SCL under quasi-equilibrium state in Section 5.2. Finally, we conduct two-dimensional (2D) phase-field simulations to study the microstructure evolution process in STO polycrystalline material during sintering and analyze the resulting grain size distribution in Section 5.3.

Note that in the paper we ignore the GB orientation dependency or other anisotropy of the segregation energies  $\Delta g_{V_{\ddot{O}}}$  and  $\Delta g_{dop}$ , for we intend to reveal the most fundamental mechanisms of SCL formation and abnormal grain growth. Without loss of generality, the proposed phase-field model can be extended accordingly to include such anisotropy aspects.

### 5.1. GB space charge layers at equilibrium

To demonstrate the capability of the phase-field model at thermodynamically equilibrium state, one-dimensional phase-field simulations are conducted and compared with the sharp interface predictions [30]. The semi-finite simulation domain has the size of 780 nm, with the core located at the left boundary. The grain boundary thickness is prescribed to be 0.78 nm [30]. The domain is discretized into a mesh consisting of 2000 elements. The simulation temperature is set at 600 K, and the relative permittivity  $\epsilon_r$  of strontium titanate (STO) is specified as 160, according to [30], which is calculated via  $\epsilon_r = 9 \times 10^4 / (T - 35)$  as mentioned in section 3.1. The interface energy, molar volume and interface mobility of STO are  $0.6 \text{ Jm}^{-2}$ ,  $3.6 \times 10^{-5} \text{ m}^3 \text{mol}^{-1}$  and  $1 \times 10^{-7} \text{ m}^3 \text{J}^{-1} \text{s}^{-1}$ , respectively [38]. The relative tolerance for convergence is set to  $1 \times 10^{-8}$ .

#### 5.1.1. Benchmark case 1: The MS Model

By fixing a uniform dopant concentration, the proposed phase-field model can be used to simulate the MS case. The results are given in Fig. 2. The initial concentrations of oxygen vacancies and dopant far from the core (denoted as  $c_{dop,b}(\infty)$  and  $c_{V_{\ddot{O}},b}(\infty)$ , respectively) are  $7 \times 10^{24} \text{ m}^{-3}$  and  $3.5 \times 10^{24} \text{ m}^{-3}$  [30]. The number of available sites of oxygen vacancy in bulk phase and GB core are  $N_{V_{\ddot{O}},b} = 5.12 \times 10^{28} \text{ m}^{-3}$  and  $N_{V_{\ddot{O}},c} = 3 \times 10^{26} \text{ m}^{-3}$ , respectively [30, 49]. The grain boundary potential  $\Phi_0$  is plotted as a function of  $\Delta g_{V_{\ddot{O}}}$  in Fig. 2(a). Due to the right boundary being grounded, the grain boundary potential is directly obtained at the interface position when  $\eta = 0.5$ , as defined in the phase-field method. For  $\Delta g_{V_{\ddot{O}}}$  larger than -1.25 eV, the phase-field results exhibit good agreement with analytical calculations. As  $\Delta g_{V_{\ddot{O}}}$  becomes more negative, particularly at -1.5 eV and -2.0 eV, the available oxygen vacancy sites are completely exhausted. Therefore, the concentrations of oxygen vacancies in the core are close to  $N_{V_{\ddot{O}},c}$ . Although the phase-field results demonstrate convergent behavior, a discrepancy between the phase-field results and the analytical solution emerges. To explain the aforementioned discrepancy, we plot the concentration of oxygen vacancies in the core as a function of  $\Delta g_{V_{\ddot{O}}}$  in Fig. 2(b). Similar to the grain boundary potential,  $c_{V_{\ddot{O}}}$  is also extracted at  $\eta = 0.5$ . We observe that the phase-field results coincide with the analytical predictions, even when  $\Delta g_{V_{\ddot{O}}} = -2.0 \text{ eV}$ . Next, we examine the concentration of oxygen vacancy in the bulk in terms of  $x$ . Here, we plot the phase-field results for  $\Delta g_{V_{\ddot{O}}} = -0.5 \text{ eV}$ , -1.0 eV and -1.5 eV in Fig. 2 (c), (d) and (e) in the range of 0 to 50 nm, which includes half of the interface region. For the analytical solution, we shift it to the right by a distance of  $w_c/2$  to match the bulk phase in the phase-field results. When  $\Delta g_{V_{\ddot{O}}} = -0.5 \text{ eV}$ ,  $c_{V_{\ddot{O}},b}$  obtained by phase-field

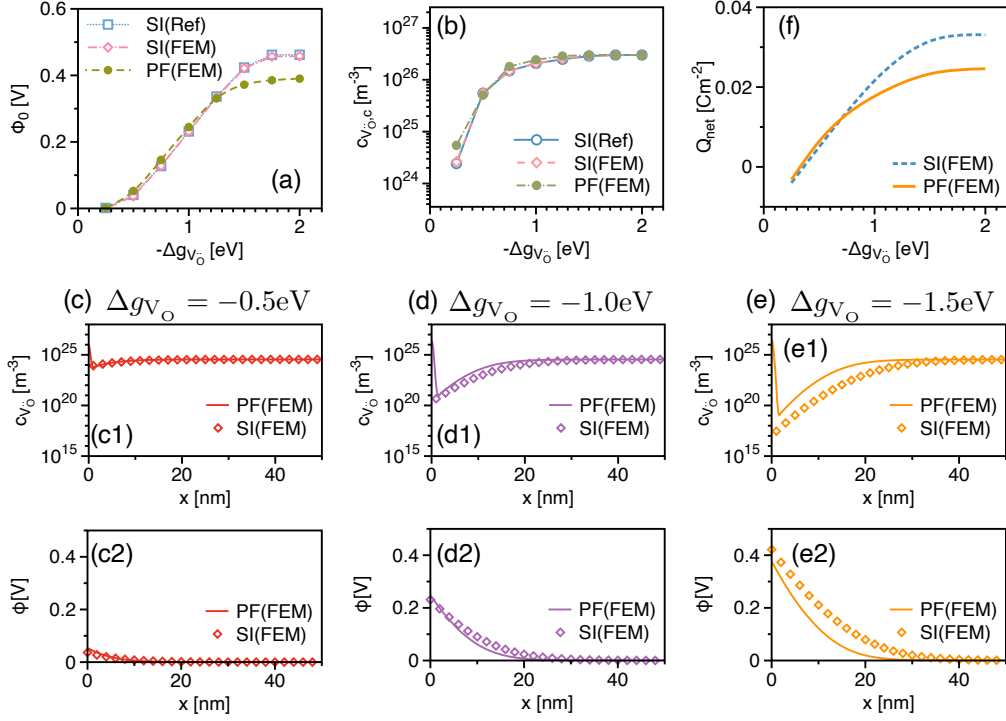


Figure 2: Comparison of phase-field (PF) simulation outcomes with those of the sharp interface (SI) model predictions obtained via FEM and taken from Ref. [30] in the MS model. Figure (a) illustrates the grain boundary potential as a function of  $\Delta g_{V_{\ddot{O}}}$ . Figure (b) depicts the relationship between the oxygen vacancy concentration and  $\Delta g_{V_{\ddot{O}}}$ . Figures (c), (d), and (e) present the concentration distribution of dopant and the electrostatic potential distribution for different oxygen vacancy segregation energy. Figure (f) demonstrates the net area density of charge in the core as a function of  $\Delta g_{V_{\ddot{O}}}$ .

simulations agrees well with analytical predictions as shown in Fig. 2(c1). However, in Fig. 2(d1) and (e1), for  $\Delta g_{V_{\ddot{O}}} = -1.5$  and  $-2.0$  eV, the phase-field results produce higher  $c_{V_{\ddot{O}},b}$ . This comparison indicates that less oxygen vacancy is segregated in the core in the phase-field simulations when choosing more negative  $\Delta g_{V_{\ddot{O}}}$ . Additionally, we plot the area density of the net charge,  $Q_{\text{net}} = \int_{-w_c/2}^{w_c/2} (z_{\text{dop}} c_{\text{dop},c} + z_{V_{\ddot{O}}} c_{V_{\ddot{O}},c}) dx$ , in the core in Fig. 2(f). Less net charge is reproduced via phase-field simulation when  $\Delta g_{V_{\ddot{O}}}$  is smaller. In short, this discrepancy is attributed to the diffuse interface in the phase-field simulations. Due to its finite interface thickness and smooth interface characteristics, the core is less positively charged compared to analytical solutions. Consequently, the electrostatic potential profile obtained via phase-field simulations decays faster than analytical calculations as shown in Fig. 2(c2), (d2) and (e2). Up to this point, we clearly observe a good agreement between the oxygen vacancy concentrations in the GB core and bulk phase as predicted by the phase-field results and the sharp interface predictions. The different approaches to handling interfaces in the phase-field model and the sharp interface method can result in discrepancies when the available densities of point defects are fully occupied.

### 5.1.2. Benchmark case 2: The GC Model

By setting the electrochemical potentials of the acceptor dopant and of the oxygen vacancies to be constant, the presented phase-field model is then reduced to the GC model, in order to reproduce the equilibrium SCL formation in the GC case. The number of available sites of dopant and oxygen vacancy in bulk and GB core are  $N_{V_{\odot},c} = 1 \times 10^{27} \text{ m}^{-3}$ ,  $N_{V_{\odot},b} = 5.12 \times 10^{28} \text{ m}^{-3}$ ,  $N_{\text{dop},c} = 1.68 \times 10^{27} \text{ m}^{-3}$  and  $N_{\text{dop},b} = 1.69 \times 10^{28} \text{ m}^{-3}$ , respectively [30, 49]. The Debye lengths  $l_D = \sqrt{\frac{\epsilon_0 \epsilon_r k_B T}{2e^2 c_{\text{dop},b}(\infty)}}$  in both MS and GC models are 5.71 nm. In Fig. 3(a), the grain boundary potentials obtained via the phase-field simulations are compared with the sharp interface predictions.  $\Delta g_{V_{\odot}}$  is fixed at -1.0 eV here.

When  $\Delta g_{\text{dop}}$  is positive, dopant cations are rejected from the core, thereby causing a more pronounced grain boundary potential. Conversely, as  $\Delta g_{\text{dop}}$  becomes negative, dopant segregation to the core occurs, reducing the net charge and consequently decreasing the grain boundary potential. Moreover, as  $\Delta g_{\text{dop}}$  becomes sufficiently negative, the available number sites for dopant segregating within the core become scarce. Therefore, the grain boundary potential profile is flat when  $\Delta g_{\text{dop}}$  is positive or sufficiently negative. The comparison indicates the phase-field results agree with the predictions of analytical solution. The discrepancy is smaller than 7%. The concentrations of vacancies and acceptor dopants in the core as a function of  $\Delta g_{\text{dop}}$  are plotted in Fig. 3(b).

In Fig. 3(c), (d), and (e), we present the concentration profiles of oxygen vacancies and dopant, as well as the distribution of electrostatic potential in the bulk phase for  $\Delta g_{\text{dop}} = 0 \text{ eV}$ , -0.125 eV and -0.375 eV, respectively. Due to symmetry, we only depict half of the SCL in one bulk phase.

At  $\Delta g_{\text{dop}} = 0 \text{ eV}$ , phase-field results predict the formation of a dopant accumulation zone near the core. The dopant concentration in the core can be much lower than in the accumulation zone, leading to the formation of a nonmonotonic curve as shown in Fig. 3(c1). Contrarily, in Virkant's findings [38], the expected accumulation zone at  $\Delta g_{\text{dop}} = 0 \text{ eV}$  is replaced by a depletion zone. As  $\Delta g_{\text{dop}}$  decreases to -0.125 eV, dopant concentration in the core increases significantly, causing the formation of monotonic concentration profile. Further decreasing  $\Delta g_{\text{dop}}$  to -0.375 eV, the dopant concentration in the core increases to  $N_{\text{dop},b}$ . It is evident that the accumulation zone becomes lower than 0 eV, more exactly -0.125 eV. Additionally, near the core, the concentration profile of dopant exhibits a distinct kink, indicating a notable change in the gradient.

The oxygen vacancy concentration profiles of are plotted in Fig. 3(c2), (d2) and (e2). Depletion appears for all  $\Delta g_{\text{dop}}$ . Notably, as  $\Delta g_{\text{dop}}$  decreases, there is an increase in the concentrations within these depletion zones. In Fig. 3(c3), (d3) and (e3), we present a comparison of the electrostatic potential across the SCL with analytical solutions. The phase-field simulation results agree well with these analytical predictions. Decreasing  $\Delta g_{\text{dop}}$  causes lower electrostatic potential distribution near the core. Moreover, we also present the net charge area density  $Q_{\text{net}}$  in Fig. 3(f). The trend of the curve obtained via phase-field results agrees with the analytical predictions. Analogous to the MS case, phase-field results are smaller than analytical predictions.

### 5.2. GB space charge layers at quasi-equilibrium

In this section, we investigate systematically the solute drag effect caused by an asymmetric SCL at a quasi-statically moving GB in a STO bicrystal. The solute drag phenomenon arises when point defects, segregated within a moving core in a quasi-equilibrium state, lead to additional free energy dissipation to maintain motion. At low core velocities, these defects can keep pace with the core, significantly increasing the necessary driving force. However, beyond a critical velocity, the defects lag behind, remaining in the bulk phases and causing the breakdown of symmetric concentration and electrostatic potential profiles across the SCL.

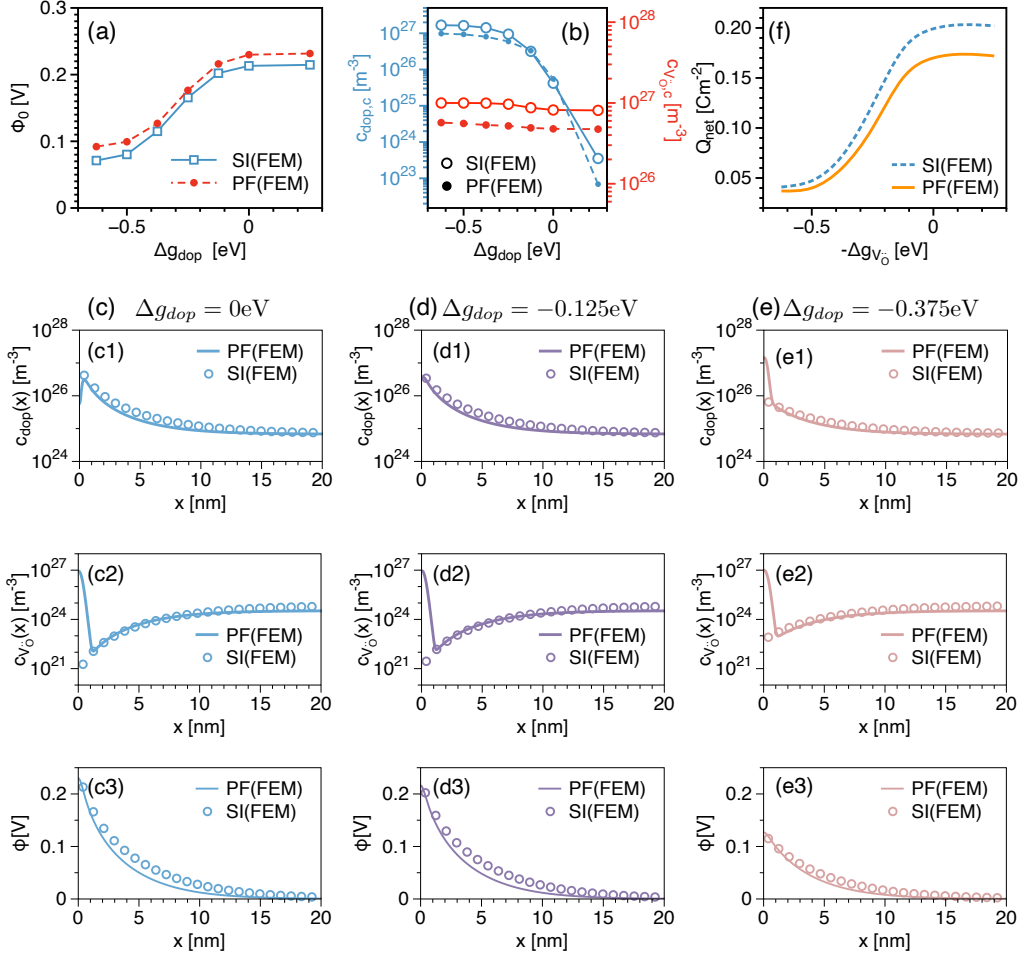


Figure 3: Comparison of phase-field (PF) simulation results with the sharp interface (SI) results via FEM method for the GC case. Figures (a) and (b) showcase the variations in grain boundary potential, dopant concentration, and oxygen vacancy concentration in the core as functions of  $\Delta g_{\text{dop}}$ . Figures (c), (d), and (e) detail the spatial distributions of dopant and oxygen vacancy concentrations in the bulk phase and the electrostatic potential. Figure (f) depicts the area density of net charge in the core, also as a function of  $\Delta g_{\text{dop}}$ .  $\Delta g_{\text{v}_\text{O}}$  was kept at -1.0 eV for all calculations.



To investigate the formation of asymmetric SCL due to solute drag effects under quasi-equilibrium conditions, a constant core velocity ( $v_c$ ) along the simulation domain is assigned as a parameter in the simulations. The velocity of the core ranges from  $0.01 \text{ nm s}^{-1}$  to  $100 \text{ nm s}^{-1}$  to study its influence on the SCL. The defect chemistry parameters  $N_{V_{\ddot{O}},c}$ ,  $N_{V_{\ddot{O}},b}$ ,  $N_{\text{dop},c}$  and  $N_{\text{dop},b}$  in this case are  $1 \times 10^{27} \text{ m}^{-3}$ ,  $5.12 \times 10^{28} \text{ m}^{-3}$ ,  $1.68 \times 10^{27} \text{ m}^{-3}$  and  $1.69 \times 10^{28} \text{ m}^{-3}$ , respectively. Simulations are conducted at 1623 K, with a relative permittivity ( $\epsilon_r$ ) of STO set to 56, based on [38]. The diffusivities of oxygen vacancies and dopant in the bulk phase are specified as  $1.35 \times 10^{-9} \text{ m}^2 \text{ s}^{-1}$  and  $1.3 \times 10^{-11} \text{ m}^2 \text{ s}^{-1}$ , respectively [38]. The simulation domain and boundary conditions remain consistent with the previous case.

In alignment with Vikrant [38], the total driving force  $F_T$  for the core motion is given by

$$F_T = \int_{-\infty}^{\infty} \frac{v_c}{L} \left( \frac{\partial \eta}{\partial x} \right)^2 dx + \int_{-\infty}^{\infty} \mu_{V_{\ddot{O}}} \frac{\partial C_{V_{\ddot{O}}}}{\partial x} dx + \int_{-\infty}^{\infty} \mu_{\text{dop}} \frac{\partial C_{\text{dop}}}{\partial x} dx. \quad (60)$$

The second and third terms in Eq. (60) denote as the electrochemical drag force, which accounts for the electrostatic and chemical contributions. The integration in Eq. (60) are solved numerically.

In Fig. 4, we illustrate the concentration profiles of oxygen vacancies and dopant, as well as the charge density and electrostatic potential as functions of  $x$ . From Fig. 4(a) to Fig. 4(e), we progressively increase the velocity of the core from  $0 \text{ nm s}^{-1}$  to  $100 \text{ nm s}^{-1}$ . The direction of the core motion is from left to right along  $x$ -axis. In the following context, the left side of the core is named as the growing grain, while the right side is called the shrinking grain.

In Fig. 4(a), the symmetric SCL formation is presented at  $v_c = 0 \text{ nm s}^{-1}$ . However, the symmetric pattern begins to deteriorate even at very low velocity, e.g.  $0.01 \text{ nm s}^{-1}$ , as shown in Fig. 4(b1), (b2) and (b3). Compared with the concentration profiles at an equilibrium state, the accumulation zone of dopant in the growing grain is reduced, while that of the shrinking grain increases. This asymmetry arises, since during the core motion, dopant cations in the shrinking grain are captured by core due to their low diffusivity. Driving the motion of extra dopant cations within the core demands extra free energy dissipation. Therefore, the dopant cations flowing from the core region into the growing grain lead to the enhancement of the accumulation zone in the growing grain. However, the concentration of dopant in the core decreases from  $7.8 \times 10^{25} \text{ m}^{-3}$  ( $v_c = 0$  in Fig. 4(a1)) to  $6.8 \times 10^{28} \text{ m}^{-3}$  at  $v_c = 0.01 \text{ nm s}^{-1}$ . In the growing grain far from the core, dopant concentration reaches  $7.2 \times 10^{25} \text{ m}^{-3}$ , which is higher than equilibrium concentration, i.e.  $c_{\text{dop},b}(\infty)$ , as shown in Fig. 4(a1). In Fig. 4(b2), we plot the calculated charge density  $\rho = e(z_{\text{dop}}c_{\text{dop}} + z_{V_{\ddot{O}}}c_{V_{\ddot{O}}})$ . The charge density in the core decreases. Compared with the equilibrium case, we also observe the formation of less (more) negative charged zone in the shrinking (growing) grain, respectively. In Fig. 4(b3), the grain boundary potential increases from  $0.248 \text{ V}$  ( $v_c = 0 \text{ nm s}^{-1}$ ) to  $0.265 \text{ V}$  at  $v_c = 0.01 \text{ nm s}^{-1}$ . Moreover, an electrostatic potential different of  $0.011 \text{ V}$  develops between the shrinking and growing grains.

When we increase the velocity of the core to  $0.5 \text{ nm s}^{-1}$ , dopant cations are not capable of catching the movement of core, as depicted in Fig. 4(c1). Consequently, the dopant concentration within the core decreases substantially, resulting in a smaller depletion zone ahead of the core and a reduced accumulation zone behind it. Similarly, the concentration of oxygen vacancies within the core also decreases significantly. Correspondingly, as shown in Fig. 4(c2), the charge density in the core drops to  $8.6 \times 10^{-7} \text{ Cm}^{-3}$ , which contrasts with the increase in charge density in the core observed in Vikrant's work [38] at intermediate velocities. We attribute the difference to the defect chemistry incorporated in the present phase field model.

When the core velocity increases to  $2 \text{ nm s}^{-1}$ , the segregation of dopant in the core becomes negligible, as shown in Fig. 4(d1). The concentration of dopant on both the left and right sides of the bulk phase returns to the equilibrium value, i.e.  $c_{\text{V}_{\text{O}},\text{b}}(\infty)$ . In Fig. 4(d2), due to the continuous decrease in charge density within the core, the negatively charged zone is diminished. Furthermore, the grain boundary potential increases to 0.446 V and the electrostatic potential difference between the left and right sides reaches 0.122 V.

At a high core velocity, such as  $100 \text{ nm s}^{-1}$ , the dopant concentration profile becomes completely flat, while the oxygen vacancy concentration profile exhibits strong asymmetry, as depicted in Fig. 4(e1). The concentration of oxygen vacancies within the core decreases significantly to  $2.46 \times 10^{26} \text{ m}^{-3}$ . In the shrinking grain, the depletion zone of oxygen vacancies remains sharp, about 2.5 nm, but it extends to approximately 20 nm in the growing grain. Consequently, as shown in Fig. 4(e2), the negatively charged zone in the shrinking grain is much smaller, and the negative charge region in the growing grain is negligible. In Fig. 4(e3), the electrostatic potential is illustrated. The grain boundary potential increases to 1.02 V and decays very slowly in the growing grain. In addition, the electrostatic potential difference becomes more pronounced, reaching 0.995 V.

In summary, at small core velocity, the asymmetric formation of SCL is mainly caused by dopant coming apart from the core. The charge density in the negatively charged SCL and in the positively charged core both decrease. As a result, the electrostatic potential in the shrinking grain increases to a positive value. At high core velocity, dopant cations do not segregate to the core. The oxygen vacancy concentration profile is strongly asymmetric. This asymmetry causes an extended diffusion layer in the growing grain and elevates the electrostatic potentials in both the core and the shrinking grain.

In order to further investigate solute drag effects and identify the critical core velocity at which a velocity jump occurs during sintering process, we present the core velocity as a function of the total driving force calculated via Eq. (60) in Fig. 5. The segregation energy difference,  $\Delta g_{\text{dop}}$  and  $\Delta g_{\text{V}_{\text{O}}}$ , allow direct tuning of the concentrations of oxygen vacancy and dopant in the core, thereby impacting the critical total driving force required for a specific core velocity. In Fig. 5(a), we hold  $\Delta g_{\text{dop}}$  and  $c_{\text{dop},\text{b}}(\infty)$  constant at -0.5 eV and  $7 \times 10^{25} \text{ m}^{-3}$  and progressively decrease  $\Delta g_{\text{V}_{\text{O}}}$  from -0.5 eV to -1.75 eV. During the grain shrinking process, the driving force resulting from the GB curvature becomes increasingly significant. Consequently, the velocity of the GB core evolves from a low value to a high value. At low core velocities, a more negative  $\Delta g_{\text{V}_{\text{O}}}$  induces higher concentration of oxygen vacancy in the core consequently demanding a larger driving force to maintain the same velocity. As the core velocity increases to  $1 \text{ nm s}^{-1}$ , the dopant cations are unable to keep pace with the core movement, resulting in a nearly flat dopant concentration within the core. Hence, this leads to the same linear relationship between the total driving force and the core velocity for different  $\Delta g_{\text{V}_{\text{O}}}$  at high velocity. On the other hand, for fixed  $\Delta g_{\text{V}_{\text{O}}}$ , such as  $\Delta g_{\text{V}_{\text{O}}} = -1.75 \text{ eV}$ , we clearly observe the velocity jumps from  $0.065 \text{ nm s}^{-1}$  to approximate  $1.5 \text{ nm s}^{-1}$  at  $1.45 \times 10^7 \text{ Nm}^{-2}$ . As we increase  $\Delta g_{\text{V}_{\text{O}}}$  to -1.0 eV, we hardly observe the velocity jump. When  $\Delta g_{\text{V}_{\text{O}}} = -0.5 \text{ eV}$ , both the concentrations of dopant and oxygen vacancy in the core decrease significantly. The solute drag effect therefore becomes negligible. Fig. 5(b) shows the influence of  $\Delta g_{\text{dop}}$  on solute drag effects when  $\Delta g_{\text{V}_{\text{O}}}$  and  $c_{\text{dop},\text{b}}$  are held constant at -1.5 eV and  $7 \times 10^{25} \text{ m}^{-3}$ . In contrast to Fig. 5(a), we can evidently observe velocity jumps for all  $\Delta g_{\text{dop}}$ . As we decrease  $\Delta g_{\text{dop}}$  to less negative value, such as from -0.2 eV to -0.3 eV, the enhancement of the solute drag effect is not significant. In Fig. 5(c), we explore the impact of the dopant concentration in the bulk far from the core, denoted as  $c_{\text{dop},\text{b}}(\infty)$ . We fix  $\Delta g_{\text{V}_{\text{O}}}$  and  $\Delta g_{\text{dop}}$  at -1.5 eV and -0.5 eV. As  $c_{\text{dop},\text{b}}(\infty)$  increases,

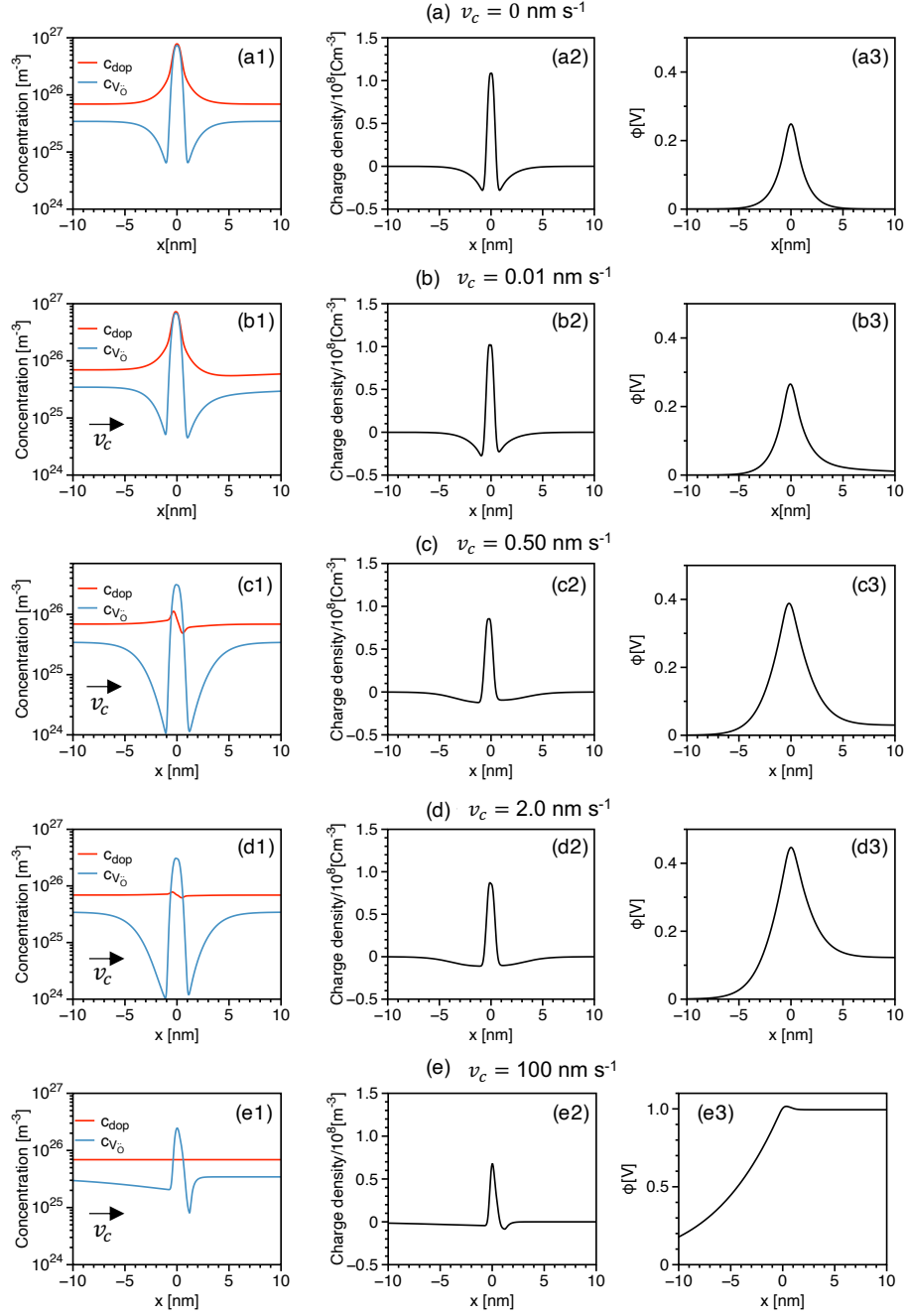


Figure 4: Asymmetric SCL formation in a STO bicrystal system with  $c_{\text{dop},b}(\infty) = 7.0 \times 10^{25} \text{ m}^{-3}$ ,  $\Delta g_{V_O} = -1.5 \text{ eV}$  and  $\Delta g_{\text{dop}} = -0.5 \text{ eV}$  at quasi-equilibrium state under different constant core velocity (a)  $v_c = 0 \text{ nm s}^{-1}$ , (b)  $v_c = 0.01 \text{ nm s}^{-1}$ , (c)  $v_c = 0.5 \text{ nm s}^{-1}$ , (d)  $v_c = 2 \text{ nm s}^{-1}$ , (e)  $v_c = 100 \text{ nm s}^{-1}$ . Each row has three sub-figures, depicting the distribution of dopant and oxygen vacancy concentrations, total charge density and electrostatic potential, respectively.

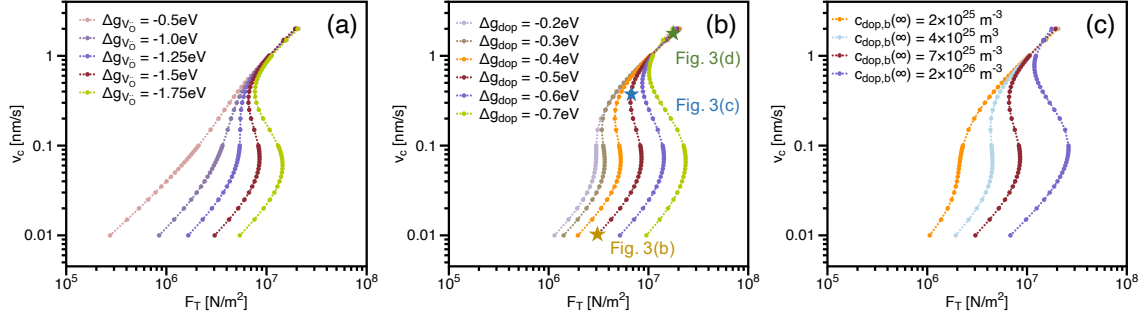


Figure 5: The total driving force on a GB with a constant velocity with (a)  $\Delta g_{dop} = -0.5$  eV,  $c_{dop,b}(\infty) = 7 \times 10^{25} \text{ m}^{-3}$  and different  $\Delta g_{V_0}$ , (b)  $\Delta g_{V_0} = -1.5$  eV,  $c_{dop,b}(\infty) = 7 \times 10^{25} \text{ m}^{-3}$  and different  $\Delta g_{dop}$ , (c)  $\Delta g_{V_0} = -1.5$  eV,  $\Delta g_{dop} = -0.5$  eV and different  $c_{dop,b}(\infty)$ . The pentagram symbols in subfigure b correspond to the different GB core velocities studied in Fig. 4. The green, blue and saffron pentagram symbols indicate  $v_c = 2 \text{ nm s}^{-1}$ ,  $0.5 \text{ nm s}^{-1}$  and  $0.01 \text{ nm s}^{-1}$ , respectively. Due to the range limit of y-axis,  $v_c = 0 \text{ nm s}^{-1}$  (Fig. 4 a) and  $100 \text{ nm s}^{-1}$  (Fig. 4 e) are not marked.

a larger driving force is necessary to counterbalance the solute drag effect to achieve the same core velocity. Additionally, a lower critical velocity is observed when the velocity jump occurs at smaller values of  $c_{dop,b}(\infty)$ . Specifically, the critical velocity increases from  $0.065 \text{ nm s}^{-1}$  to  $0.095 \text{ nm s}^{-1}$ , as  $c_{dop,b}(\infty)$  is raised from  $4 \times 10^{25} \text{ m}^{-3}$  to  $2 \times 10^{26} \text{ m}^{-3}$ .

In the sintering process, the driving forces are initially large and decrease as the grain size increases. In other words, the GB core velocity starts on the upper right side of the S-shaped curves in Fig. 5 at the initial stage of the grain growth. As the grain size increases, the GB core velocity decreases to the critical velocity. At this point, a transition from high velocity to low velocity occurs at the critical value. In Fig. 5(a), we observe GB core velocity jumps when  $\Delta g_{V_0} = -1.5$  eV and  $-1.75$  eV. The critical velocities for different  $\Delta g_{V_0}$  are approximately  $0.35 \text{ nm s}^{-1}$ . Additionally, the GB core velocity jumps to a lower value when  $\Delta g_{V_0}$  is more negative. In Fig. 5(b), the critical GB core velocity increases from  $0.15 \text{ nm s}^{-1}$  to  $0.65 \text{ nm s}^{-1}$  as  $\Delta g_{dop}$  decreases from  $-0.3$  eV to  $-0.7$  eV. In Fig. 5(c), a larger  $c_{dop,b}(\infty)$  leads to a higher critical velocity.

### 5.3. Abnormal grain growth

After systematically benchmarks and knowledge gained from quasi-static single GB cases, we investigate different abnormal grain growth patterns of materials with different defect segregation energies  $\Delta g_{dop}$ ,  $\Delta g_{V_0}$  and bulk defect concentrations such as  $c_{dop,b}$ . The segregation of point defects in the core plays a significant role in influencing grain growth kinetics. To investigate the grain size distribution of STO polycrystalline material after sintering, we conduct 2D phase-field simulations. Note that three-dimensional phase-field simulations of the proposed model are achievable but require significantly more computational resources, which will be considered in the near future. In fact, to reveal the fundamental mechanisms, 2D simulations should be sufficient and allow for a comprehensive parameter study given the limited computational resources.

The simulation box size is set to  $390 \text{ nm} \times 390 \text{ nm}$  with a grid resolution of  $1000 \times 1000$  points. The polycrystalline microstructure is initialized using a Voronoi tessellation method, where each grain was assigned a unique grain index. We started with an initial number of 1000 grains, and the random seed used for generating the polycrystalline microstructure is set to 42. To optimize

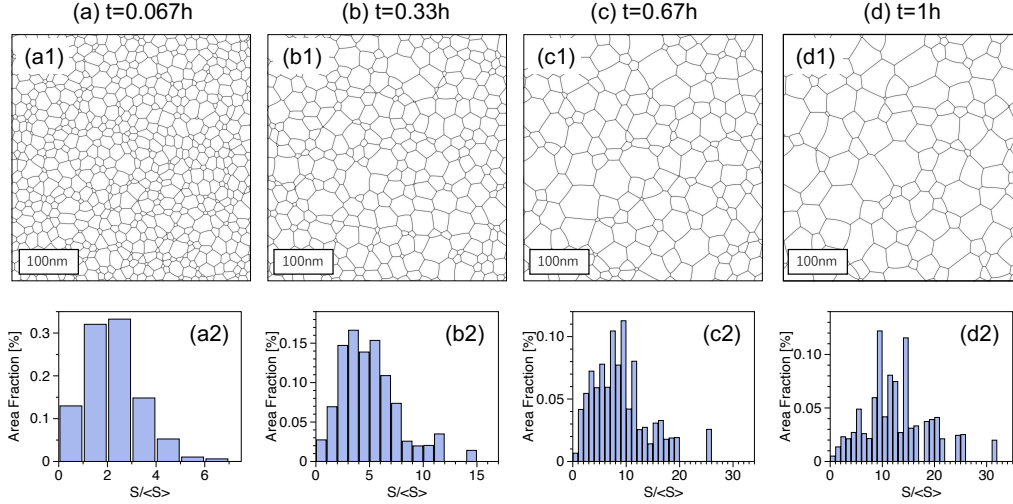


Figure 6: The microstructure evolution of grain growth process at (a) 0.067 h, (b) 0.33 h, (c) 0.67 h and (d) 1 h, with defect chemistry parameters set at  $\Delta g_{V_{\odot}} = -1.5$  eV,  $\Delta g_{\text{dop}} = -0.4$  eV and  $c_{\text{dop},b} = 7 \times 10^{25} \text{ m}^{-3}$ . These parameters are consistent with those used in Fig. 7(e). By 1h, a bimodal grain size distribution becomes apparent.

memory usage during simulations, we also utilize grain tracker algorithm [34]. In the simulations, we set  $N_{V_{\odot},c}$ ,  $N_{V_{\odot},b}$ ,  $N_{\text{dop},c}$  and  $N_{\text{dop},b}$  as  $1 \times 10^{27} \text{ m}^{-3}$ ,  $5.12 \times 10^{28} \text{ m}^{-3}$ ,  $1.68 \times 10^{27} \text{ m}^{-3}$  and  $1.69 \times 10^{28} \text{ m}^{-3}$ . The simulations are conducted at a temperature of 1623 K, where the non-Arrhenius behavior of the grain growth is found [28]. Periodic boundary conditions are applied to all edges of the simulation domain for the phase-fields and concentration fields. For the electrostatic potential field, the bottom-left corner is grounded, while the other edges are set with the periodic boundary conditions. Furthermore, all the parameters used in the simulation are normalized. The lattice constant  $a = 3.9 \times 10^{-10} \text{ m}$  is used for the length normalization. Other normalization factors include e.g.  $f_0 = \kappa/a^2 = 2.3 \times 10^9 \text{ Jm}^{-3}$  for the energy density,  $t_0 = 1/(Lf_0) = 0.0043 \text{ s}$  for the interface mobility, and  $\phi_0 = f_0 V_m / \mathcal{F} = 0.858 \text{ V}$  for the electrostatic potential.

We present first the microstructure evolution of the grain growth process under specific conditions  $\Delta g_{V_{\odot}} = -1.5$  eV,  $\Delta g_{\text{dop}} = -0.4$  eV and  $c_{\text{dop},b} = 7 \times 10^{25} \text{ m}^{-3}$  when the sintering time is  $t/h = \{0.067, 0.33, 0.67, 1.0\}$ . The average area of grain at time  $t = 0$  is  $\langle S \rangle$ , i.e.,  $152.1 \text{ nm}^2$ . When  $t = 0.067 \text{ h}$ ,  $0.33 \text{ h}$  and  $0.67 \text{ h}$ , the grain size increases while the area fraction of small grain decreases. The grain size distribution starts to transition from a mono-modal to a bimodal pattern. When  $t = 1 \text{ h}$ , the largest grain area is about 32 times larger than  $\langle S \rangle$ . The bimodal grain size distribution is clearly visible.

### 5.3.1. Influence of segregation energies and bulk defect concentration

Subsequently, we investigate the influence of defect chemistry parameters on the microstructure evolution during sintering processes. The microstructure of grains is presented in Fig. 7(a)-(g) after 1 hour of sintering at 1623 K. In Fig. 7(a), (b) and (c), we increase  $\Delta g_{V_{\odot}}$  from -1.5 eV to -0.5 eV when  $\Delta g_{\text{dop}} = -0.5$  eV and  $c_{\text{dop},b} = 7 \times 10^{25} \text{ m}^{-3}$ . Bimodal grain size distribution is clearly observed in Fig. 7(a2), (b2) and (c2). As  $\Delta g_{V_{\odot}}$  becomes more negative, the peak in the range of  $0 < \frac{S}{\langle S \rangle} < 4$  induced by smaller grains becomes more pronounced. As predicted in Fig. 5(a),

solute drag effect is almost negligible for  $\Delta g_{V_{\text{O}}} = -0.5$  eV. Nonetheless, the formation of solute cloud imprinted by vanished GBs is still detectable in Fig. 7(c3) even though the solute drag effect is very weak. Concentration of oxygen vacancy is detailed in Fig. 7(a4), (b4) and (c4). Segregation is more significant for  $\Delta g_{V_{\text{O}}} = -1.5$  eV. Compared to the dopant, solute cloud of oxygen vacancies are less distinct. In view of the higher diffusivity of oxygen vacancy, the contribution of oxygen vacancy to solute drag force is also weak. Solute clouds of oxygen vacancies are only observed near the junctions where grains shrink rapidly with a small radius. The electrostatic potential distributions are depicted in Fig. 7(a5), (b5) and (c5). The negative potential bands can be also observed near the GB cores. As all the considered cases show, the electrostatic potentials in small shrinking grains are significantly higher than in the surrounding growing grains, leading to a stronger electrostatic contribution to the solute drag effects. Consequently, the shrinking speed of small grains is reduced, which induces pinning effects on the surrounding growing grains. Note that the heterogeneous electrostatic potential distribution arises from the velocity difference of individual GB, in accordance to the observation in the quasi-static cases in Fig. 4, rather than any anisotropy which is absent in the current simulations.

In Fig. 7(a), (d) and (e), we keep  $\Delta g_{V_{\text{O}}}$  and  $c_{\text{dop},b}$  at  $-1.5$  eV and  $7 \times 10^{25} \text{ m}^{-3}$  and test different  $\Delta g_{\text{dop}}$  values. Whereas, in Fig. 7(a), (f) and (g),  $\Delta g_{V_{\text{O}}}$  and  $\Delta g_{\text{dop}}$  are constant while  $c_{\text{dop},b}$  increases from  $2 \times 10^{25} \text{ m}^{-3}$  to  $2 \times 10^{26} \text{ m}^{-3}$ . For all simulations, the solute drag effects from dopant are pronounced. The dopant clouds imprinted by vanished GBs are clearly observed behind GB cores. In Fig. 7(e2) and (g2), the bimodal grain size distributions are presented. However, when  $\Delta g_{\text{dop}} = -0.6$  eV in Fig. 7(d2) and  $c_{\text{dop},b} = 2 \times 10^{26} \text{ m}^{-3}$  in Fig. 7(f2), the unimodal grain size distribution exhibits, due to the more pronounced probability of small grain. The simulation results in Fig. 7(f) demonstrate the high grain number, where the large grains are surrounded by small grains.

### 5.3.2. Grain boundary potential distribution

In Fig. 8, we present the statistics of the average grain boundary potential in the GB core, denoted as  $\bar{\phi}_{\text{core}}$ . The value of  $\bar{\phi}_{\text{core}}$  is calculated as an average of the electrostatic potential along the GB core indicated by  $\eta_i = 0.5$  over individual GB length. Fig. 8(a) illustrates the distribution of  $\bar{\phi}_{\text{core}}$  for  $\Delta g_{V_{\text{O}}} = -0.5$  eV,  $\Delta g_{\text{dop}} = -0.5$  eV,  $c_{\text{dop}}(\infty) = 7 \times 10^{25} \text{ m}^{-3}$  (refer to Fig. 7(c) for the associated phase-field simulation result). When the solute drag effect is negligible,  $\bar{\phi}_{\text{core}}$  is smaller than 0.05 V and approximately follows the normal distribution. In Fig. 8(b), the distribution of  $\bar{\phi}_{\text{core}}$  is presented for  $\Delta g_{V_{\text{O}}} = -1.5$  eV,  $\Delta g_{\text{dop}} = -0.5$  eV,  $c_{\text{dop}}(\infty) = 7 \times 10^{25} \text{ m}^{-3}$  (refer to Fig. 7(a)). Here,  $\bar{\phi}_{\text{core}}$  significantly increases. In addition, the distribution of  $\bar{\phi}_{\text{core}}$  changes from mono-modal to bimodal, with one peak at 0.31 V and another at 0.35 V. In Fig. 8(c), the parameters  $\Delta g_{V_{\text{O}}} = -1.5$  eV,  $\Delta g_{\text{dop}} = -0.5$  eV,  $c_{\text{dop}}(\infty) = 2 \times 10^{26} \text{ m}^{-3}$  are chosen (refer to Fig. 7(f)). In this case, the solute drag effect is the most pronounced in this study. Not only  $\bar{\phi}_{\text{core}}$  increases but also the bimodal distribution of  $\bar{\phi}_{\text{core}}$  becomes more distinct.

In addition, two distinct types of GBs can be observed Fig. 9. The first type, characterized by a lower moving velocity, exhibits nearly symmetric concentration profiles across the GB core with a significantly higher segregation concentration of dopant. However, within a polycrystalline system, the accumulation zone of dopant at the space charge region transitions into a depletion zone. Conversely, the second type of GB core, which moves at a higher velocity, shows lower dopant concentrations due to the break of the symmetric SCL. Similarly, the oxygen vacancy distribution in this second GB core is also asymmetric, as illustrated in Fig. 7(e). Fig. 7(f) presents the electrostatic potential distributions across these two types of GB cores, where the second GB core displays a



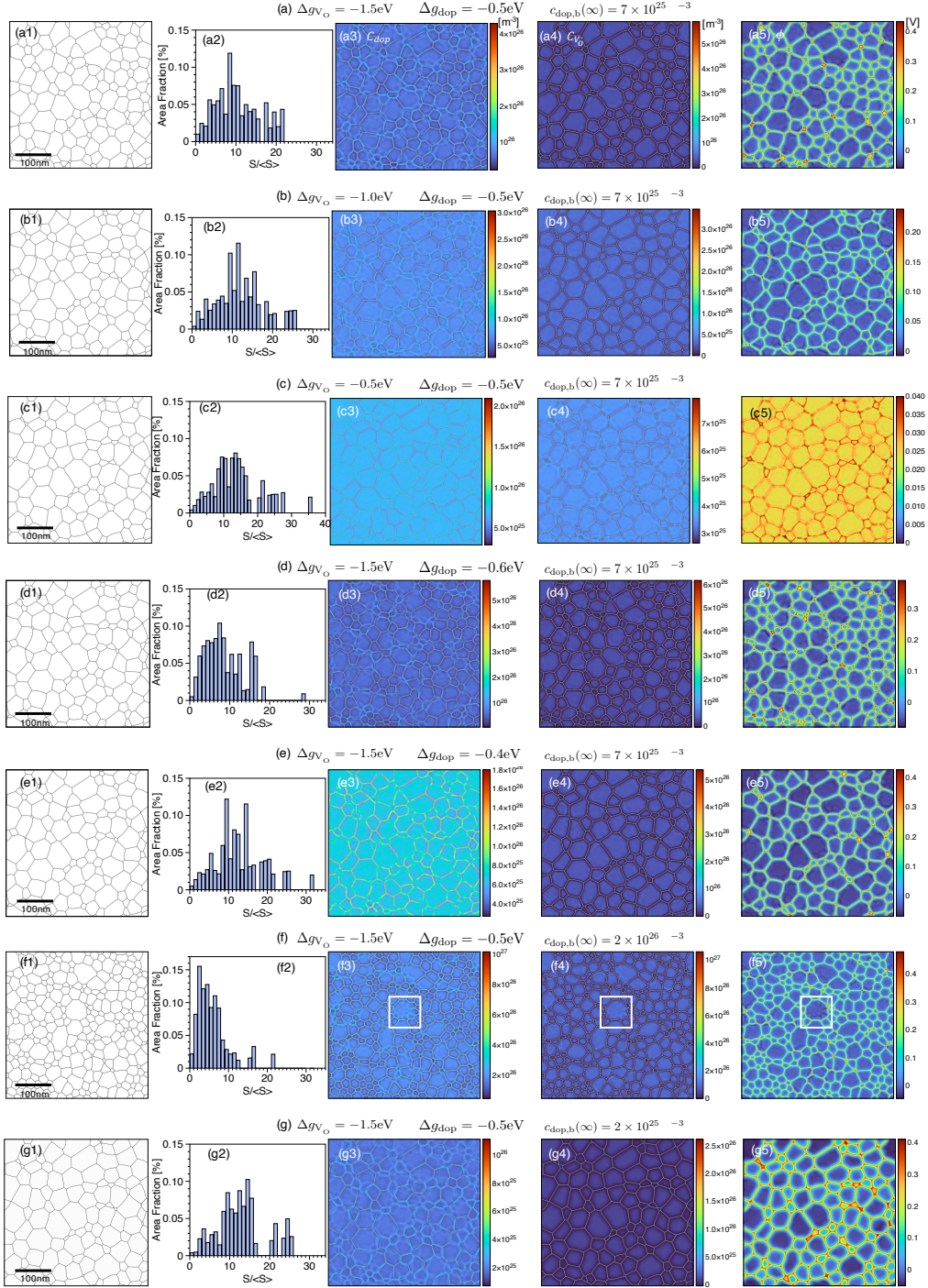


Figure 7: Phase-field simulation results of abnormal grain growth in Fe-doped STO after 1 h sintering under the influence of different defect chemistry parameters.

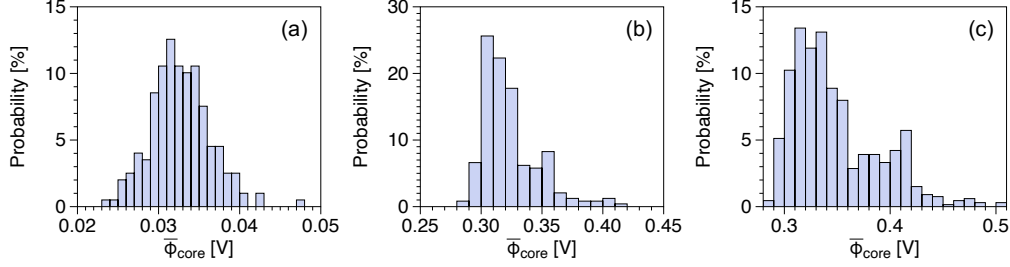


Figure 8: Probability of the average grain boundary potential in the GB cores with different defect chemistry parameters (a)  $\Delta g_{V_{\text{O}}} = -0.5$  eV,  $\Delta g_{\text{dop}} = -0.5$  eV,  $c_{\text{dop}}(\infty) = 7 \times 10^{25} \text{ m}^{-3}$  (refer to Fig. 7(c)), (b)  $\Delta g_{V_{\text{O}}} = -1.5$  eV,  $\Delta g_{\text{dop}} = -0.5$  eV,  $c_{\text{dop}}(\infty) = 7 \times 10^{25} \text{ m}^{-3}$  (refer to Fig. 7(a)), (c)  $\Delta g_{V_{\text{O}}} = -1.5$  eV,  $\Delta g_{\text{dop}} = -0.5$  eV,  $c_{\text{dop}}(\infty) = 2 \times 10^{26} \text{ m}^{-3}$  (refer to Fig. 7(f)).

larger grain boundary potential and a more pronounced electrostatic potential difference.

In order to further evidence the two types of GB core, 14 different GBs are selected from the rectangular region in Fig. 7 (f). The relations between  $v_c$  and  $F_T$  as well as  $\bar{\phi}_{\text{core}}$  and  $F_T$  for each GB core are represented in Fig. 10(b). Here,  $F_T$  is the total driving force, numerically calculated via Eq. (60). The solid lines indicate the phase-field simulation results in the bicrystal case (refer to the purple line in Fig. 5(c)), while the symbols represent different GBs in the polycrystalline case. In Fig. 10(b), the relationships of  $F_T$  vs.  $v_c$  and  $F_T$  vs.  $\bar{\phi}_{\text{core}}$  in the polycrystalline case almost follow those in the bicrystal case. There is also a velocity jump and an electrostatic potential jump when the total driving force is approximately  $2 \times 10^7 \text{ N/m}^2$ . In the high GB velocity region, GB6, GB7 and GB8, with less dopant segregation, have much higher electrostatic potentials than the others, aligning well with the predictions in the bicrystal case. In the low GB velocity region, GB3, GB13 and GB14 also agree well with the results from the bicrystal quasi-static case. Whereas, GBs with higher velocities, such as GB2, GB4, GB11 and GB12, do not fit well into the S curve of a bicrystal case. This discrepancy can be attributed to multiple reasons. For instance, these GBs have higher GB curvatures and can interact with other GBs, which go beyond the bicrystal model and can only be resolved by the grain growth simulations presented here.

## 6. Conclusion

In this work, we develop a phase-field model to investigate SCL formation during grain growth in oxide electroceramics based firmly on principles of the defect chemistry. The main results of the paper include:

- The proposed phase-field model reproduces a series of benchmark results at equilibrium of Fe-doped STO bicrystal. Simulation results, including the symmetric SCLs, grain boundary potentials, concentrations of oxygen vacancies and acceptor dopants in the GB core and the bulk phase as well as the electrostatic distributions, show good agreement with the analytical predictions in the MS and GC models.
- Simulations are carried out comprehensively for a GB core moving with constant velocities under quasi-equilibrium state. At low core velocity, the accumulation zone in the shrinking grain decreases, while it increases in the growing grain, leading to the asymmetric SCL



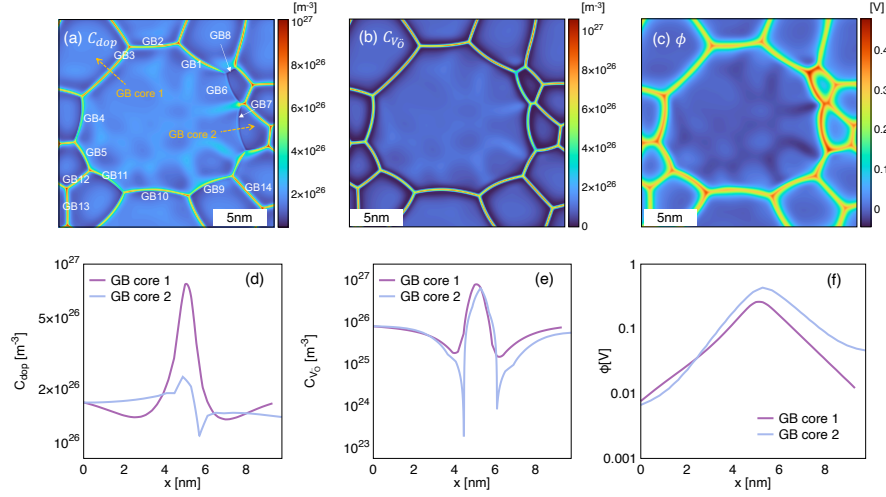


Figure 9: Two types of GBs are observed in the rectangular region highlighted in Fig. 7(f). The distributions of dopant concentration, oxygen vacancy concentration, and electrostatic potential in this region are shown in (a), (b), and (c), respectively. Particularly, the dopant concentration profile within the grain interior in (a) exhibits strong imprints of vanished GBs during sintering. Two types of GB cores are distinguished by dashed yellow lines in (a). The first type, characterized by a low moving velocity, has a higher segregation concentration of dopants. In contrast, the second type, with a higher core velocity, shows a lower and asymmetric dopant concentration across the GB core. Furthermore, the dopant concentration, oxygen vacancy concentration, and electrostatic potential along the two types of GB cores are plotted in (d), (e), and (f), respectively.

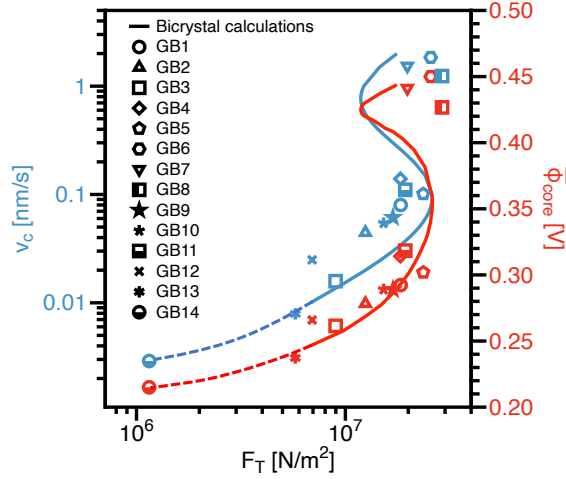


Figure 10: GB core velocity  $v_c$  and average grain boundary potential  $\bar{\phi}_{core}$  as functions of the total driving force  $F_T$ . The 14 different GBs, shown in Fig. 9(a), are chosen from the rectangular region in Fig. 7(f) in polycrystalline simulations. The relations between  $v_c$  and  $F_T$  as well as  $\bar{\phi}_{core}$  and  $F_T$  are obtained from phase-field simulations in bicrystal and polycrystalline Fe-doped STO. Solid lines indicate the simulation results for the bicrystal case, while dashed lines are the extrapolations of the simulation results in bicrystal case at very low GB velocity regime. Other symbols represent 14 different GBs chosen in the polycrystalline case.

formation. With increasing GB core velocity, the dopant segregation diminishes. However, the movement of oxygen vacancy within the GB core only breaks at extremely high velocity due to the high diffusivity of oxygen vacancy. In addition, the electrostatic potential in the shrinking grain becomes higher than that in the growing grain.

- Abnormal grain growth is observed even without distinguishing any grain orientation or considering any anisotropic GB mobility in the phase-field simulations at 1623K. It indicates that the solute drag effect alone can lead to bimodal grain size distribution. As the formation energy differences of oxygen vacancies and acceptor dopants ( $\Delta g_{V_{\text{O}}}$  and  $\Delta g_{\text{dop}}$ ) become more negative, the grain growth velocity decreases. This trend is also observed with increasing dopant concentration ( $c_{\text{dop,b}}$ ). Notably, the dopant concentration profile within the grain interior distinctly reflects the significant imprint of the grain boundaries that disappeared during sintering.
- Simulation results reveal two distinct types of GB cores. The first type, with nearly symmetric concentration profiles at the GB, exhibits stronger solute drag effects, resulting in a much lower moving velocity and a tendency to remain pinned in position. The second type of GB core shows asymmetric concentration profiles and a higher moving velocity, contributing predominantly to grain coarsening.
- Abnormal grain growth resulting from solute drag effects leads to a large variation of grain boundary potentials. Typically, smaller grains exhibit higher grain boundary potentials at the later stages of grain growth and form more blocking GBs in term of ionic conductivity. When considering the total conductivity of an electrolyte material, the electrical current needs to find a "detour" around these blocking GBs by passing through the surrounding larger grains, with less blocking GBs. It implies that to increase the conductivity one may also optimize the microstructure so that blocking GBs can be circumvented more easily. In contrast, if blocking GBs are desired, such as in capacitors, the grain size should be kept small to prevent the development of detour paths.

The proposed phase-field model offers naturally a series of promising extensions. We can e.g. incorporate additional species, such as neutral dopants, electrons, and electron holes, into the current phase-field model to quantitatively investigate the formation of the SCL. Furthermore, GB orientation plays a crucial role in SCL formation, and both the interface energy and the defect chemistry parameters  $\Delta g_{V_{\text{O}}}$  and  $\omega_c N_{V_{\text{O}},c}$  depend on GB orientation [49]. These complexities can be included in the phase-field model in the near future. Moreover, we assume in this paper only the  $\text{Fe}^{3+}$  and ignore  $\text{Fe}^{4+}$ , which is reasonable for high temperature scenarios. But, the situation regarding solute drag effect changes at low temperature when a significant amount of  $\text{Fe}^{4+}$  is present. The  $\text{Fe}^{3+}$  ions in the GB core can not easily follow the movement of the GB core due to their low diffusivity. In contrast, the rapid movement of electron holes can adjust the local  $\text{Fe}^{3+}/\text{Fe}^{4+}$  ratio and establish an equilibrium charge distribution. The solute drag effect may differ when a significant amount of  $\text{Fe}^{4+}$  is considered.

## Acknowledgement

The financial support of German Science Foundation (DFG) in the framework of the Collaborative Research Centre 1548 (CRC 1548, project number 463184206) and the Project 471260201 are

acknowledged. The authors K. Wang and B.-X. Xu greatly appreciate the access to the Lichtenberg II High-Performance Computer (HPC) and the technique supports from the HHLR, Technische Universität Darmstadt. The computing time on the HPC is granted by the NHR4CES Resource Allocation Board under the project “special00007”.

## References

- [1] T. Ishihara, H. Matsuda, Y. Takita, Doped LaGaO<sub>3</sub> perovskite type oxide as a new oxide ionic conductor, *J. Am. Chem. Soc.* 116 (9) (1994) 3801–3803.
- [2] K.-D. Kreuer, Proton-conducting oxides, *Annu. Rev. Mater. Res.* 33 (1) (2003) 333–359.
- [3] Z. Wang, Z. Liu, G. Zhao, Z. Zhang, X. Zhao, X. Wan, Y. Zhang, Z. L. Wang, L. Li, Stretchable unsymmetrical piezoelectric BaTiO<sub>3</sub> composite hydrogel for triboelectric nanogenerators and multimodal sensors, *ACS nano* 16 (1) (2022) 1661–1670.
- [4] N. Y. Chan, M. Zhao, J. Huang, K. Au, M. H. Wong, H. M. Yao, W. Lu, Y. Chen, C. W. Ong, H. L. W. Chan, et al., Highly sensitive gas sensor by the LaAlO<sub>3</sub>/SrTiO<sub>3</sub> heterostructure with Pd nanoparticle surface modulation, *Adv. Mater.* 26 (34) (2014) 5962–5968.
- [5] S. W. Lee, J. H. Han, S. Han, W. Lee, J. H. Jang, M. Seo, S. K. Kim, C. Dussarrat, J. Gatineau, Y.-S. Min, et al., Atomic layer deposition of SrTiO<sub>3</sub> thin films with highly enhanced growth rate for ultrahigh density capacitors, *Chem. Mater.* 23 (8) (2011) 2227–2236.
- [6] C. Hou, W. Huang, W. Zhao, D. Zhang, Y. Yin, X. Li, Ultrahigh energy density in SrTiO<sub>3</sub> film capacitors, *ACS Appl. Mater. Interfaces* 9 (24) (2017) 20484–20490.
- [7] A. Kursumovic, E. Defay, O. J. Lee, C.-F. Tsai, Z. Bi, H. Wang, J. L. MacManus-Driscoll, A new material for high-temperature lead-free actuators, *Adv. Funct. Mater.* 23 (47) (2013) 5881–5886.
- [8] S.-H. Baek, C.-B. Eom, Epitaxial integration of perovskite-based multifunctional oxides on silicon, *Acta Mater.* 61 (8) (2013) 2734–2750.
- [9] R. Muenstermann, T. Menke, R. Dittmann, R. Waser, Coexistence of filamentary and homogeneous resistive switching in Fe-doped SrTiO<sub>3</sub> thin-film memristive devices, *Adv. Mater.* 22 (43) (2010) 4819–4822.
- [10] Z. Hu, Q. Li, M. Li, Q. Wang, Y. Zhu, X. Liu, X. Zhao, Y. Liu, S. Dong, Ferroelectric memristor based on Pt/BiFeO<sub>3</sub>/Nb-doped SrTiO<sub>3</sub> heterostructure, *Appl. Phys. Lett.* 102 (10) (2013).
- [11] T. P. Mishra, S. Wang, C. Lenser, D. Jennings, M. Kindelmann, W. Rheinheimer, C. Broeckmann, M. Bram, O. Guillon, Ultra-fast high-temperature sintering of strontium titanate, *Acta Mater.* 231 (2022) 117918.
- [12] M. J.-H. Reavley, H. Guo, J. Yuan, A. Y. R. Ng, T. Y. K. Ho, H. T. Tan, Z. Du, C. L. Gan, Ultrafast high-temperature sintering of barium titanate ceramics with colossal dielectric constants, *J. Eur. Ceram. Soc.* 42 (12) (2022) 4934–4943.
- [13] M. Sayer, K. Sreenivas, Ceramic thin films: fabrication and applications, *Science* 247 (4946) (1990) 1056–1060.

- [14] H. Li, X. Hu, Y. Wei, Z. Yu, X. Zhang, R. Droopad, A. Demkov, J. Edwards Jr, K. Moore, W. Ooms, et al., Two-dimensional growth of high-quality strontium titanate thin films on Si, *J. Appl. Phys.* 93 (8) (2003) 4521–4525.
- [15] R. Chaim, M. Levin, A. Shlayer, C. Estournès, Sintering and densification of nanocrystalline ceramic oxide powders: a review, *Adv. Appl. Ceram.* 107 (3) (2008) 159–169.
- [16] J. Maier, *Physical chemistry of ionic materials: ions and electrons in solids*, John Wiley & Sons, 2023.
- [17] D. M. Smyth, *The defect chemistry of metal oxides*, 2000.
- [18] F. Kröger, H. Vink, Relations between the concentrations of imperfections in crystalline solids, in: *Solid State Phys.*, Vol. 3, Elsevier, 1956, pp. 307–435.
- [19] J. P. Parras, R. A. De Souza, Grain-boundary diffusion of cations in fluorite-type oxides is faster but not always easier, *Acta Mater.* 195 (2020) 383–391.
- [20] R. Sažinas, I. Sakaguchi, M.-A. Einarsrud, T. Grande, 134Ba diffusion in polycrystalline BaMO<sub>3</sub> (M= Ti, Zr, Ce), *AIP Adv.* 7 (11) (2017).
- [21] R. Waser, R. Hagenbeck, Grain boundaries in dielectric and mixed-conducting ceramics, *Acta Mater.* 48 (4) (2000) 797–825.
- [22] J. W. Cahn, The impurity-drag effect in grain boundary motion, *Acta Metall.* 10 (9) (1962) 789–798.
- [23] M. Hillert, B. Sundman, A treatment of the solute drag on moving grain boundaries and phase interfaces in binary alloys, *Acta Metall.* 24 (8) (1976) 731–743.
- [24] S. G. Kim, Y. B. Park, Grain boundary segregation, solute drag and abnormal grain growth, *Acta Mater.* 56 (15) (2008) 3739–3753.
- [25] M. P. Zahler, S. M. Kraschewski, H. Stoermer, D. Gerthsen, M. Baeurer, W. Rheinheimer, Grain growth and segregation in Fe-doped SrTiO<sub>3</sub>: Experimental evidence for solute drag, *J. Eur. Ceram. Soc.* 43 (4) (2023) 1613–1624.
- [26] D. Jennings, M. P. Zahler, D. Wang, Q. Ma, W. Deibert, M. Kindelmann, C. Kübel, S. Baumann, O. Guillon, J. Mayer, et al., Grain boundary segregation in iron doped strontium titanate: From dilute to concentrated solid solutions, *Acta Mater.* 273 (2024) 119941.
- [27] W. Rheinheimer, M. J. Hoffmann, Grain growth in perovskites: What is the impact of boundary transitions?, *Curr. Opin. Solid State Mater. Sci.* 20 (5) (2016) 286–298.
- [28] W. Rheinheimer, M. J. Hoffmann, Non-arrhenius behavior of grain growth in strontium titanate: New evidence for a structural transition of grain boundaries, *Scr. Mater.* 101 (2015) 68–71.
- [29] J. Fleig, The grain boundary impedance of random microstructures: numerical simulations and implications for the analysis of experimental data, *Solid State Ion.* 150 (1-2) (2002) 181–193.

- [30] R. A. De Souza, The formation of equilibrium space-charge zones at grain boundaries in the perovskite oxide  $\text{SrTiO}_3$ , *Phys. Chem. Chem. Phys.* 11 (43) (2009) 9939–9969.
- [31] K. Wang, G. Boussinot, C. Hüter, E. A. Brener, R. Spatschek, Modeling of dendritic growth using a quantitative nondiagonal phase field model, *Phys. Rev. Mater.* 4 (3) (2020) 033802.
- [32] K. Wang, G. Boussinot, E. A. Brener, R. Spatschek, Quantitative nondiagonal phase field modeling of eutectic and eutectoid transformations, *Phys. Rev. B* 103 (18) (2021) 184111.
- [33] V. Rehn, J. Hötzer, W. Rheinheimer, M. Seiz, C. Serr, B. Nestler, Phase-field study of grain growth in porous polycrystals, *Acta Mater.* 174 (2019) 439–449.
- [34] Y. Yang, O. Ragnvaldsen, Y. Bai, M. Yi, B.-X. Xu, 3D non-isothermal phase-field simulation of microstructure evolution during selective laser sintering, *npj Comput. Mater.* 5 (1) (2019) 81.
- [35] Y. Yang, T. D. Oyediji, P. Kühn, B.-X. Xu, Investigation on temperature-gradient-driven effects in unconventional sintering via non-isothermal phase-field simulation, *Scr. Mater.* 186 (2020) 152–157.
- [36] Y. Yang, M. Fathidoost, T. D. Oyediji, P. Bondi, X. Zhou, H. Egger, B.-X. Xu, A diffuse-interface model of anisotropic interface thermal conductivity and its application in thermal homogenization of composites, *Scr. Mater.* 212 (2022) 114537.
- [37] T. D. Oyediji, Y. Yang, H. Egger, B.-X. Xu, Variational quantitative phase-field modeling of nonisothermal sintering process, *Phys. Rev. E* 108 (2) (2023) 025301.
- [38] K. Vikrant, W. Rheinheimer, R. E. García, Electrochemical drag effect on grain boundary motion in ionic ceramics, *npj Comput. Mater.* 6 (1) (2020) 165.
- [39] K. Vikrant, W. Rheinheimer, H. Sternlicht, M. Bäurer, R. E. García, Electrochemically-driven abnormal grain growth in ionic ceramics, *Acta Mater.* 200 (2020) 727–734.
- [40] X. Tong, D. S. Mebane, R. A. De Souza, Analyzing the grain-boundary resistance of oxide-ion conducting electrolytes: Poisson-Cahn vs Poisson-Boltzmann theories, *J. Am. Ceram. Soc.* 103 (1) (2020) 5–22.
- [41] S. G. Kim, W. T. Kim, T. Suzuki, Phase-field model for binary alloys, *Phys. Rev. E* 60 (6) (1999) 7186.
- [42] R. Merkle, W. Sitte, J. Maier, Water incorporation into materials with three mobile carriers: Two-fold relaxation of the electromotive force in Fe-doped  $\text{SrTiO}_3$  and importance of hole trapping, *Solid State Ion.* 347 (2020) 115174.
- [43] N. Moelans, B. Blanpain, P. Wollants, Quantitative analysis of grain boundary properties in a generalized phase field model for grain growth in anisotropic systems, *Phys. Rev. B* 78 (2) (2008) 024113.
- [44] Y. Bai, Y. Zhao, W. Liu, B.-X. Xu, Two-level modeling of lithium-ion batteries, *J. Power Sources* 422 (2019) 92–103.

- [45] T. J. Hughes, The finite element method: linear static and dynamic finite element analysis, Courier Corporation, 2012.
- [46] S. C. Brenner, The mathematical theory of finite element methods, Springer, 2008.
- [47] D. Schwen, L. Agesen, J. Peterson, M. Tonks, Rapid multiphase-field model development using a modular free energy based approach with automatic differentiation in moose/marmot, *Comput. Mater. Sci.* 132 (2017) 36–45. doi:<https://doi.org/10.1016/j.commatsci.2017.02.017>.  
URL <https://www.sciencedirect.com/science/article/pii/S0927025617300885>
- [48] G. Giudicelli, A. Lindsay, L. Harbour, C. Icenhour, M. Li, J. E. Hansel, P. German, P. Behne, O. Marin, R. H. Stogner, J. M. Miller, D. Schwen, Y. Wang, L. Munday, S. Schunert, B. W. Spencer, D. Yushu, A. Recuero, Z. M. Prince, M. Nezdyur, T. Hu, Y. Miao, Y. S. Jung, C. Matthews, A. Novak, B. Langley, T. Truster, N. Nobre, B. Alger, D. Andrš, F. Kong, R. Carlsen, A. E. Slaughter, J. W. Peterson, D. Gaston, C. Permann, 3.0 - MOOSE: Enabling massively parallel multiphysics simulations, *SoftwareX* 26 (2024) 101690. doi:<https://doi.org/10.1016/j.softx.2024.101690>.  
URL <https://www.sciencedirect.com/science/article/pii/S235271102400061X>
- [49] R. De Souza, E. Dickey, The effect of space-charge formation on the grain-boundary energy of an ionic solid, *Phil. Trans. R. Soc. A* 377 (2152) (2019) 20180430.

# Supplementary Information: A defect-chemistry-informed phase-field model of grain growth in oxide electroceramics

Kai Wang<sup>1</sup>, Roger A. De Souza<sup>2</sup>, Xiang-Long Peng<sup>1</sup>, Rotraut Merkle<sup>3</sup>, Wolfgang Rheinheimer<sup>4</sup>, Karsten Albe<sup>5</sup>, and Bai-Xiang Xu<sup>\*1</sup>

<sup>1</sup>Mechanics of Functional Materials Division, Institute of Materials Science, Technische Universität Darmstadt, Darmstadt, 64287, Germany

<sup>2</sup>Institute of Physical Chemistry, RWTH Aachen University, Aachen, 52056, Germany

<sup>3</sup>Max Planck Institute for Solid State Research, Heisenbergstraße 1, Stuttgart, 70569, Germany

<sup>4</sup>University of Stuttgart, Institute for Manufacturing Technologies of Ceramic Components and Composites (IFKB), Stuttgart, 70569, Germany

<sup>5</sup>Materials Modelling Division, Institute of Materials Science, Technische Universität Darmstadt, Darmstadt, 64287, Germany

## 1 Implementation of analytical calculations via Finite element method (FEM)

The analytical solution for the space charge layer formation in STO at equilibrium state is achieved using the finite element method (FEM) in both one and two dimensions within the Multiphysics Object-Oriented Simulation Environment (MOOSE) framework. For both MS and GC models, a semi-infinite simulation domain parallel to the x-axis is chosen. The location of the core is set at the left boundary ( $x = 0$ ). As for the boundary conditions, the electrostatic field is grounded at the right side, i.e.,  $\phi|_{x=\infty} = 0$ , while at the left side, a nonlinear boundary condition is given by

$$\left. \frac{\partial \phi}{\partial x} \right|_{x=0} = -\frac{Q_c(\phi_0)}{2\epsilon_0\epsilon_r}, \quad (S1)$$

where  $Q_c(\phi_0) = ew_c(z_{V\ddot{O}}c_{V\ddot{O},c} + z_{dop}c_{dop,c})$  and  $\phi_0 = \phi|_{x=0}$ . In MS model,  $c_{V\ddot{O},c}$  is calculated via

$$c_{V\ddot{O},c} = \frac{N_{V\ddot{O},c}c_{V\ddot{O},b}(\infty) \exp\left[-\frac{\Delta g_{V\ddot{O}} + z_{V\ddot{O}}e\Phi_0}{k_B T}\right]}{N_{V\ddot{O},b} + c_{V\ddot{O},b}(\infty) \exp\left[-\frac{\Delta g_{V\ddot{O}} + z_{V\ddot{O}}e\Phi_0}{k_B T}\right]}, \quad (S2)$$

and  $c_{dop,c}$  is set to  $c_{dop,b}(\infty)$ . In GC model,  $c_{dop,c}$  is a function of  $x$ , calculated via

$$c_{dop,c} = \frac{N_{dop,c}c_{dop,b}(\infty) \exp\left[-\frac{\Delta g_{dop} + z_{dop}e\Phi_0}{k_B T}\right]}{N_{dop,b} + c_{dop,b}(\infty) \exp\left[-\frac{\Delta g_{dop} + z_{dop}e\Phi_0}{k_B T}\right]}. \quad (S3)$$

The analytical calculations are performed previously in a referenced study based on an iterative procedure to determine the space charge potential. However, we introduce the boundary condition, Eq. (S1), by using the modified Robin boundary condition in MOOSE framework. As a result, the space charge potential can be obtained directly without any iterative procedure, which leads to more efficient computations. The parameters used in MS and GC cases are tabulated in Table 1.

---

\*Corresponding author

Table 1: Parameters used in analytical calculations for GC and MS models

Parameters	MS Model	GC Model	Unit
$w_c$	$7.8 \times 10^{-10}$	$7.8 \times 10^{-10}$	m
$c_{\text{dop},b}(\infty)$	$7.0 \times 10^{24}$	$7.0 \times 10^{24}$	$\text{m}^{-3}$
$c_{V_{\ddot{O}},b}(\infty)$	$3.5 \times 10^{24}$	$3.5 \times 10^{24}$	$\text{m}^{-3}$
$N_{V_{\ddot{O}},c}$	$3 \times 10^{26}$	$1 \times 10^{27}$	$\text{m}^{-3}$
$N_{V_{\ddot{O}},b}$	$5.12 \times 10^{28}$	$5.12 \times 10^{28}$	$\text{m}^{-3}$
$N_{\text{dop},c}$	-	$1.68 \times 10^{27}$	$\text{m}^{-3}$
$N_{\text{dop},b}$	-	$(w_c/2)^{-3} = 1.69 \times 10^{28}$	$\text{m}^{-3}$
$\Delta g_{V_{\ddot{O}}}$	-	-3.0	eV
T	600	600	K
$\epsilon_r$	160	160	-

## 2 Analytical solution of space charge layer formation in a STO bicrystal at equilibrium state

In this section, we analyze the formation of the space charge layer in a STO bicrystal under equilibrium conditions using FEM, considering both MS and GC cases.

### 2.1 MS model

In Fig. 1, we present a comparison between the FEM results and the published data by De Souza for the MS case. In this scenario,  $c_{\text{dop},b}(x)$  remains constant across the entire calculation domain, i.e.  $c_{\text{dop},b}(x) = c_{\text{dop},b}(\infty)$ . In Fig. 1(a), the space charge potential, denoted as  $\Phi_0$ , is depicted as a function of the parameter  $\Delta g_{V_{\ddot{O}}}$ . As  $\Delta g_{V_{\ddot{O}}}$  increases, the space charge potential  $\phi_0$  also increases. However, for a fixed bulk oxygen vacancy concentration of  $N_{V_{\ddot{O}},c} = 3 \times 10^{26} \text{m}^{-3}$ , the space charge potential becomes convergent when  $\Delta g_{V_{\ddot{O}}}$  is lower than -1.5eV. This convergence occurs because all available sites of oxygen vacancies in the core become occupied, as demonstrated in Fig. 1(b). Specifically, when  $\Delta g_{V_{\ddot{O}}} = -2\text{eV}$ , we observe that  $c_{V_{\ddot{O}},c} \approx N_{V_{\ddot{O}},c}$ . The space charge potentials and concentration of oxygen vacancy in the core obtained from the FEM results for different  $\Delta g_{V_{\ddot{O}}}$  exhibit good agreement with De Souza's calculated results. In Fig. 1(c) and Fig. 1(d), the concentration of oxygen vacancy in the bulk phase and the electrostatic potential are portrayed as functions of  $x$  for different  $\Delta g_{V_{\ddot{O}}}$ . Observations from these figures reveal the presence of a depletion zone near the core region, with its length increasing significantly as  $\Delta g_{V_{\ddot{O}}}$  decreases.

#### 2.1.1 GC model

In Fig. 2, analytical solutions for the GC case are presented with  $\Delta g_{V_{\ddot{O}}}$  fixed at -3.0eV, ensuring full occupation of available oxygen vacancy sites within the core. We investigate the influence of varying  $\Delta g_{\text{dop}}$  on space charge formation. In Fig. 2(a), the space charge potential is plotted as a function of  $\Delta g_{\text{dop}}$ . When  $\Delta g_{\text{dop}}$  is positive, dopant atoms are rejected from the core, This results in a concentration of dopant in the core even smaller than  $c_{\text{dop},b}(\infty)$ , i.e.  $7 \times 10^{24} \text{m}^{-3}$ , as shown in Fig. 2(b), thereby causing a more pronounced space charge potential. Conversely, as  $\Delta g_{\text{dop}}$  becomes negative, dopant segregation within the core occurs, reducing the net charge and consequently decreasing the space charge potential. Moreover, as  $\Delta g_{\text{dop}}$  becomes sufficiently negative, the available number sites for dopant segregating within the core become scarce. As shown in Fig. 2(b),  $c_{\text{dop},b}$  approaches very close to  $N_{V_{\ddot{O}},b}$ . Consequently, the space charge potential converges.

In Fig. 2(c), concentration profiles of dopants and oxygen vacancies for different  $\Delta g_{\text{dop}}$  are presented. For all cases, the net charge in the core is positive due to a high concentration of segregated oxygen vacancies, necessitating a negatively charged space charge layer to compensate. As a result, in the vicinity of the core, depletion zone appears in the  $c_{V_{\ddot{O}},b}$  profiles, whereas the accumulation zone forms in the  $c_{\text{dop},b}$  profiles. Moreover, with larger  $\Delta g_{\text{dop}}$  values, the accumulation zone in the  $c_{\text{dop},b}$  profiles becomes more pronounced. Consequently, the electrostatic potential decreases as  $\Delta g_{\text{dop}}$  decreases and approaches convergence.



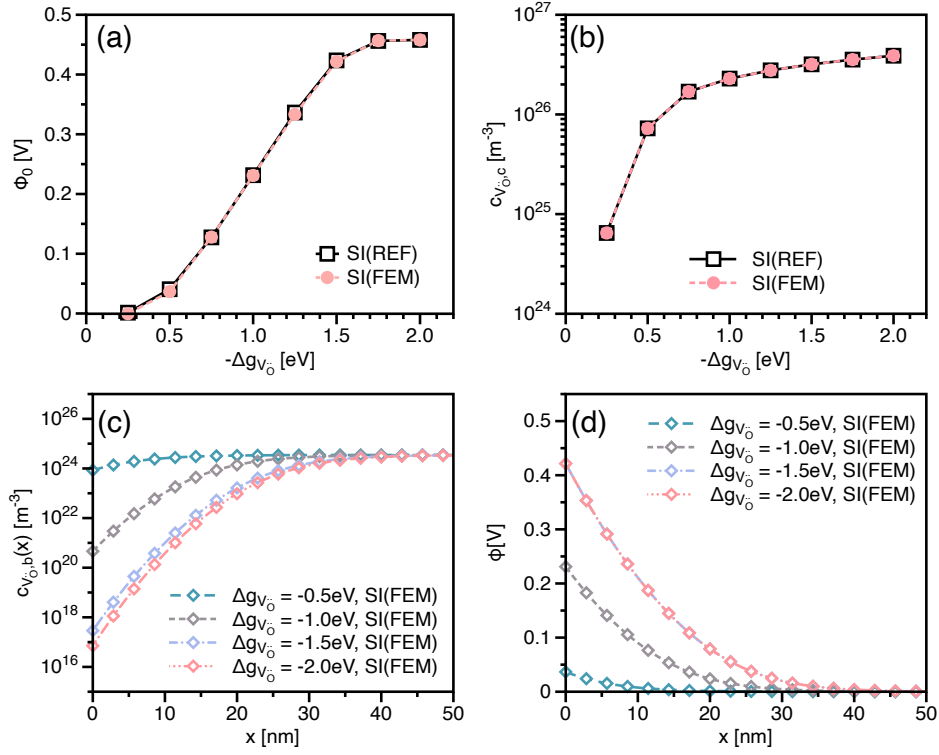


Figure 1: Comparison of analytical calculation results of via FEM and taken from Ref. [1] in MS model

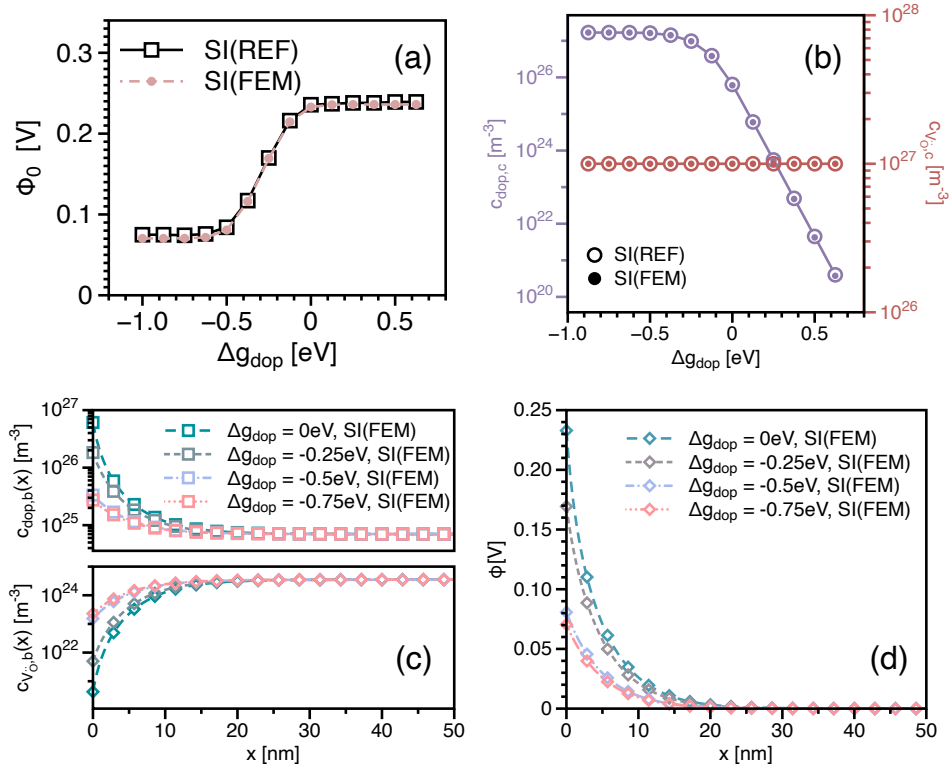


Figure 2: Comparison of analytical calculation results of via FEM and taken from Ref. [1] in GC model

### 3 Finite element implementation of the phase field model

The linearization of the residuals given in Eqs. (49) to (58) can be written in the following element-level linear formulation

$$\begin{bmatrix} R_{C_{V\ddot{O},c}}^I \\ R_{C_{\text{dop},c}}^I \\ R_{\eta_i}^I \\ R_{C_{V\ddot{O}}}^I \\ R_{C_{\text{dop}}}^I \\ R_{\mu_{V\ddot{O}}}^I \\ R_{\mu_{\text{dop}}}^I \\ R_{C_{V\ddot{O},b}}^I \\ R_{C_{\text{dop},b}}^I \\ R_{\phi}^I \end{bmatrix} = - \begin{bmatrix} K_{C_{V\ddot{O},c},C_{V\ddot{O},c}}^{IJ} & K_{C_{V\ddot{O},c},C_{\text{dop},c}}^{IJ} & K_{C_{V\ddot{O},c},\eta_i}^{IJ} & \cdots & K_{C_{V\ddot{O},c},C_{\text{dop},b}}^{IJ} & K_{C_{V\ddot{O},c},\phi}^{IJ} \\ K_{C_{\text{dop},c},C_{V\ddot{O},c}}^{IJ} & K_{C_{\text{dop},c},C_{\text{dop},c}}^{IJ} & K_{C_{\text{dop},c},\eta_i}^{IJ} & \cdots & K_{C_{\text{dop},c},C_{\text{dop},b}}^{IJ} & K_{C_{\text{dop},c},\phi}^{IJ} \\ K_{\eta_i,C_{V\ddot{O},c}}^{IJ} & K_{\eta_i,C_{\text{dop},c}}^{IJ} & K_{\eta_i,\eta_i}^{IJ} & \cdots & K_{\eta_i,C_{\text{dop},b}}^{IJ} & K_{\eta_i,\phi}^{IJ} \\ \vdots & \vdots & \vdots & \ddots & \vdots & \vdots \\ K_{\text{dop},b,C_{V\ddot{O},c}}^{IJ} & K_{\text{dop},b,C_{\text{dop},c}}^{IJ} & K_{\text{dop},b,\eta_i}^{IJ} & \cdots & K_{\text{dop},b,C_{\text{dop},b}}^{IJ} & K_{\text{dop},b,\phi}^{IJ} \\ K_{\phi,C_{V\ddot{O},c}}^{IJ} & K_{\phi,C_{\text{dop},c}}^{IJ} & K_{\phi,\eta_i}^{IJ} & \cdots & K_{\phi,C_{\text{dop},b}}^{IJ} & K_{\phi,\phi}^{IJ} \end{bmatrix} \begin{bmatrix} \delta C_{V\ddot{O},c}^I \\ \delta C_{\text{dop},c}^I \\ \delta \eta_i^I \\ \delta C_{V\ddot{O}}^I \\ \delta C_{\text{dop}}^I \\ \delta \mu_{V\ddot{O}}^I \\ \delta \mu_{\text{dop}}^I \\ \delta C_{V\ddot{O},b}^I \\ \delta C_{\text{dop},b}^I \\ \delta \phi^I \end{bmatrix} \quad (\text{S4})$$

Then, we give the non-zero terms in Eq. (59)

$$K_{C_{V\ddot{O},c},C_{V\ddot{O},c}}^{IJ} = - \int_V N_{C_{V\ddot{O},c}}^I h(\eta) N_{C_{V\ddot{O},c}}^J dV \quad (S5)$$

$$K_{C_{V\ddot{O},c},\eta_i}^{IJ} = \int_V N_{C_{V\ddot{O},c}}^I \left[ \frac{\partial h(\eta)}{\partial \eta_i} N_{\eta_i}^J C_{V\ddot{O},b} - \frac{\partial h(\eta)}{\partial \eta_i} N_{\eta_i}^J C_{V\ddot{O},c} \right] dV \quad (S6)$$

$$K_{C_{V\ddot{O},c},C_{V\ddot{O}}}^{IJ} = \int_V N_{C_{V\ddot{O},c}}^I N_{C_{V\ddot{O}}}^J dV \quad (S7)$$

$$K_{C_{V\ddot{O},c},C_{V\ddot{O},b}}^{IJ} = \int_V N_{C_{V\ddot{O},c}}^I [1 - h(\eta)] N_{C_{V\ddot{O},b}}^J dV \quad (S8)$$

$$K_{C_{\text{dop},c},C_{\text{dop},c}}^{IJ} = - \int_V N_{C_{\text{dop},c}}^I h(\eta) N_{C_{\text{dop},c}}^J dV \quad (S9)$$

$$K_{C_{\text{dop},c},\eta_i}^{IJ} = \int_V N_{C_{\text{dop},c}}^I \left[ \frac{\partial h(\eta)}{\partial \eta_i} N_{\eta_i}^J C_{\text{dop},b} - \frac{\partial h(\eta)}{\partial \eta_i} N_{\eta_i}^J C_{\text{dop},c} \right] dV \quad (S10)$$

$$K_{C_{\text{dop},c},C_{\text{dop}}}^{IJ} = \int_V N_{C_{\text{dop},c}}^I N_{C_{\text{dop}}}^J dV \quad (S11)$$

$$K_{C_{\text{dop},c},C_{\text{dop},b}}^{IJ} = \int_V N_{C_{\text{dop},c}}^I [1 - h(\eta)] N_{C_{\text{dop},b}}^J dV \quad (S12)$$

$$K_{\eta_i,C_{V\ddot{O},c}}^{IJ} = -L \int_V N_{\eta_i}^I \frac{\partial h(\eta)}{\partial \eta_i} \left[ -\frac{\partial f_c^{\text{ech}}}{\partial C_{V\ddot{O},c}} N_{C_{V\ddot{O},c}}^J + \frac{\partial f_b^{\text{ech}}}{\partial C_{V\ddot{O},b}} N_{C_{V\ddot{O},c}}^J \right] dV \quad (S13)$$

$$K_{\eta_i,C_{\text{dop},c}}^{IJ} = -L \int_V N_{\eta_i}^I \frac{\partial h(\eta)}{\partial \eta_i} \left[ -\frac{\partial f_c^{\text{ech}}}{\partial C_{\text{dop},c}} N_{C_{\text{dop},c}}^J + \frac{\partial f_b^{\text{ech}}}{\partial C_{\text{dop},b}} N_{C_{\text{dop},c}}^J \right] dV \quad (S14)$$

$$\begin{aligned} K_{\eta_i,\eta_i}^{IJ} &= L \int_V N_{\eta_i}^I \omega \frac{\partial^2 f^{\text{loc}}(\eta)}{\partial \eta_i^2} N_{\eta_i}^J + L \int_V \kappa N_{\eta_i,j}^J N_{\eta_i,j}^I dV - L \int_{\Gamma} \kappa N_{\eta_i,j}^J N_{\eta_i,j}^I \hat{n}_i d\Gamma \\ &\quad - L \int_V N_{\eta_i}^I \frac{\partial^2 h(\eta)}{\partial \eta_i^2} N_{\eta_i}^J \left[ f_b^{\text{ech}} - f_c^{\text{ech}} - \frac{\partial f_b^{\text{ech}}}{\partial C_{V\ddot{O},b}} (C_{V\ddot{O},b} - C_{V\ddot{O},c}) - \frac{\partial f_b^{\text{ech}}}{\partial C_{\text{dop},b}} (C_{\text{dop},b} - C_{\text{dop},c}) \right] dV \end{aligned} \quad (S15)$$

$$K_{\eta_i,C_{V\ddot{O},b}}^{IJ} = -L \int_V N_{\eta_i}^I \frac{\partial h(\eta)}{\partial \eta_i} \left[ -\frac{\partial f_c^{\text{ech}}}{\partial C_{V\ddot{O},b}} N_{C_{V\ddot{O},b}}^J + \frac{\partial f_b^{\text{ech}}}{\partial C_{V\ddot{O},b}} N_{C_{V\ddot{O},b}}^J \right] dV \quad (S16)$$

$$K_{\eta_i,C_{\text{dop},b}}^{IJ} = -L \int_V N_{\eta_i}^I \frac{\partial h(\eta)}{\partial \eta_i} \left[ -\frac{\partial f_c^{\text{ech}}}{\partial C_{\text{dop},b}} N_{C_{\text{dop},b}}^J + \frac{\partial f_b^{\text{ech}}}{\partial C_{\text{dop},b}} N_{C_{\text{dop},b}}^J \right] dV \quad (S17)$$

$$\begin{aligned} K_{\eta_i,\phi}^{IJ} &= -L \int_V N_{\eta_i}^I \frac{\partial h(\eta)}{\partial \eta_i} \left[ \frac{\partial f_b^{\text{ech}}}{\partial \phi} N_{\phi}^J - \frac{\partial f_c^{\text{ech}}}{\partial \phi} N_{\phi}^J \right. \\ &\quad \left. - \frac{\partial^2 f_b^{\text{ech}}}{\partial C_{V\ddot{O},b} \partial \phi} (C_{V\ddot{O},b} - C_{V\ddot{O},c}) N_{\phi}^J - \frac{\partial^2 f_b^{\text{ech}}}{\partial C_{\text{dop},b} \partial \phi} (C_{\text{dop},b} - C_{\text{dop},c}) N_{\phi}^J \right] dV \end{aligned} \quad (S18)$$

$$K_{C_{V\ddot{O}},C_{V\ddot{O},c}}^{IJ} = - \int_V N_{C_{V\ddot{O}}}^I \left( \frac{\partial^2 \mathcal{F}}{\partial C_{V\ddot{O},b} \partial C_{V\ddot{O},c}} N_{C_{V\ddot{O},c}}^J \right) dV \quad (S19)$$

$$K_{C_{V\ddot{O}},C_{\text{dop},c}}^{IJ} = - \int_V N_{C_{V\ddot{O}}}^I \left( \frac{\partial^2 \mathcal{F}}{\partial C_{V\ddot{O},b} \partial C_{\text{dop},c}} N_{C_{\text{dop},c}}^J \right) dV \quad (S20)$$

$$K_{C_{V\ddot{O}},\eta_i}^{IJ} = - \int_V N_{C_{V\ddot{O}}}^I \left( \frac{\partial^2 \mathcal{F}}{\partial C_{V\ddot{O},b} \partial \eta_i} N_{\eta_i}^J \right) dV \quad (S21)$$

$$K_{C_{V\ddot{O}},\mu_{V\ddot{O}}}^{IJ} = \int_V N_{C_{V\ddot{O}}}^I N_{\mu_{V\ddot{O}}}^J dV \quad (S22)$$

$$K_{C_{V\ddot{O}},C_{V\ddot{O},b}}^{IJ} = - \int_V N_{C_{V\ddot{O}}}^I \left( \frac{\partial^2 \mathcal{F}}{\partial C_{V\ddot{O},b} \partial C_{V\ddot{O},b}} N_{C_{V\ddot{O},b}}^J \right) dV \quad (S23)$$

$$K_{C_{V\ddot{O}},C_{\text{dop},b}}^{IJ} = - \int_V N_{C_{V\ddot{O}}}^I \left( \frac{\partial^2 \mathcal{F}}{\partial C_{V\ddot{O},b} \partial C_{\text{dop},b}} N_{C_{\text{dop},b}}^J \right) dV \quad (S24)$$

$$K_{C_{V\ddot{O}},\phi}^{IJ} = - \int_V N_{C_{V\ddot{O}}}^I \left( \frac{\partial^2 \mathcal{F}}{\partial C_{V\ddot{O},b} \partial \phi} N_{\phi}^J \right) dV \quad (S25)$$

$$K_{C_{\text{dop}}, C_{V\ddot{O},c}}^{IJ} = - \int_V N_{C_{\text{dop}}}^I \left( \frac{\partial^2 \mathcal{F}}{\partial C_{\text{dop},b} \partial C_{V\ddot{O},c}} N_{C_{V\ddot{O},c}}^J \right) dV \quad (\text{S26})$$

$$K_{C_{\text{dop}}, C_{\text{dop},c}}^{IJ} = - \int_V N_{C_{\text{dop}}}^I \left( \frac{\partial^2 \mathcal{F}}{\partial C_{\text{dop},b} \partial C_{\text{dop},c}} N_{C_{\text{dop},c}}^J \right) dV \quad (\text{S27})$$

$$K_{C_{\text{dop}}, \eta_i}^{IJ} = - \int_V N_{C_{\text{dop}}}^I \left( \frac{\partial^2 \mathcal{F}}{\partial C_{\text{dop},b} \partial \eta_i} N_{\eta_i}^J \right) dV \quad (\text{S28})$$

$$K_{C_{\text{dop}}, \mu_{\text{dop}}}^{IJ} = \int_V N_{C_{\text{dop}}}^I N_{\mu_{\text{dop}}}^J dV \quad (\text{S29})$$

$$K_{C_{\text{dop}}, C_{V\ddot{O},b}}^{IJ} = - \int_V N_{C_{\text{dop}}}^I \left( \frac{\partial^2 \mathcal{F}}{\partial C_{\text{dop},b} \partial C_{V\ddot{O},b}} N_{C_{V\ddot{O},b}}^J \right) dV \quad (\text{S30})$$

$$K_{C_{\text{dop}}, C_{\text{dop},b}}^{IJ} = - \int_V N_{C_{\text{dop}}}^I \left( \frac{\partial^2 \mathcal{F}}{\partial C_{\text{dop},b} \partial C_{\text{dop},b}} N_{C_{\text{dop},b}}^J \right) dV \quad (\text{S31})$$

$$K_{C_{\text{dop}}, \phi}^{IJ} = - \int_V N_{C_{\text{dop}}}^I \left( \frac{\partial^2 \mathcal{F}}{\partial C_{\text{dop},b} \partial \phi} N_{\phi}^J \right) dV \quad (\text{S32})$$

$$K_{\mu_{V\ddot{O}}, C_{V\ddot{O},c}}^{IJ} = \int_V \frac{\partial M_{V\ddot{O}}}{\partial C_{V\ddot{O},c}} N_{C_{V\ddot{O},c}}^J \mu_{V\ddot{O},i} N_{\mu_{V\ddot{O}}}^I dV - \int_{\Gamma} \frac{\partial M_{V\ddot{O}}}{\partial C_{V\ddot{O},c}} N_{C_{V\ddot{O},c}}^J \mu_{V\ddot{O},i} N_{\mu_{V\ddot{O}}}^I \hat{n}_i d\Gamma \quad (\text{S33})$$

$$K_{\mu_{V\ddot{O}}, C_{\text{dop},c}}^{IJ} = \int_V \frac{\partial M_{V\ddot{O}}}{\partial C_{\text{dop},c}} N_{C_{\text{dop},c}}^J \mu_{V\ddot{O},i} N_{\mu_{V\ddot{O}}}^I dV - \int_{\Gamma} \frac{\partial M_{V\ddot{O}}}{\partial C_{\text{dop},c}} N_{C_{\text{dop},c}}^J \mu_{V\ddot{O},i} N_{\mu_{V\ddot{O}}}^I \hat{n}_i d\Gamma \quad (\text{S34})$$

$$K_{\mu_{V\ddot{O}}, \mu_{V\ddot{O}}}^{IJ} = \int_V M_{V\ddot{O}} N_{V\ddot{O},i}^J N_{\mu_{V\ddot{O},i}}^I dV - \int_{\Gamma} M_{V\ddot{O}} N_{V\ddot{O},i}^J N_{\mu_{V\ddot{O},i}}^I \hat{n}_i d\Gamma \quad (\text{S35})$$

$$K_{\mu_{V\ddot{O}}, C_{V\ddot{O},b}}^{IJ} = \int_V \frac{\partial M_{V\ddot{O}}}{\partial C_{V\ddot{O},b}} N_{C_{V\ddot{O},b}}^J \mu_{V\ddot{O},i} N_{\mu_{V\ddot{O}}}^I dV - \int_{\Gamma} \frac{\partial M_{V\ddot{O}}}{\partial C_{V\ddot{O},b}} N_{C_{V\ddot{O},b}}^J \mu_{V\ddot{O},i} N_{\mu_{V\ddot{O}}}^I \hat{n}_i d\Gamma \quad (\text{S36})$$

$$K_{\mu_{V\ddot{O}}, C_{\text{dop},b}}^{IJ} = \int_V \frac{\partial M_{V\ddot{O}}}{\partial C_{\text{dop},b}} N_{C_{\text{dop},b}}^J \mu_{V\ddot{O},i} N_{\mu_{V\ddot{O}}}^I dV - \int_{\Gamma} \frac{\partial M_{V\ddot{O}}}{\partial C_{\text{dop},b}} N_{C_{\text{dop},b}}^J \mu_{V\ddot{O},i} N_{\mu_{V\ddot{O}}}^I \hat{n}_i d\Gamma \quad (\text{S37})$$

$$K_{\mu_{\text{dop}}, C_{V\ddot{O},c}}^{IJ} = \int_V \frac{\partial M_{\text{dop}}}{\partial C_{V\ddot{O},c}} N_{C_{V\ddot{O},c}}^J \mu_{\text{dop},i} N_{\mu_{\text{dop},i}}^I dV - \int_{\Gamma} \frac{\partial M_{\text{dop}}}{\partial C_{V\ddot{O},c}} N_{C_{V\ddot{O},c}}^J \mu_{\text{dop},i} N_{\mu_{\text{dop},i}}^I \hat{n}_i d\Gamma \quad (\text{S38})$$

$$K_{\mu_{\text{dop}}, C_{\text{dop},c}}^{IJ} = \int_V \frac{\partial M_{\text{dop}}}{\partial C_{\text{dop},c}} N_{C_{\text{dop},c}}^J \mu_{\text{dop},i} N_{\mu_{\text{dop},i}}^I dV - \int_{\Gamma} \frac{\partial M_{\text{dop}}}{\partial C_{\text{dop},c}} N_{C_{\text{dop},c}}^J \mu_{\text{dop},i} N_{\mu_{\text{dop},i}}^I \hat{n}_i d\Gamma \quad (\text{S39})$$

$$K_{\mu_{\text{dop}}, \mu_{\text{dop}}}^{IJ} = \int_V M_{\text{dop}} N_{\text{dop},i}^J N_{\mu_{\text{dop},i}}^I dV - \int_{\Gamma} M_{\text{dop}} N_{\text{dop},i}^J N_{\mu_{\text{dop},i}}^I \hat{n}_i d\Gamma \quad (\text{S40})$$

$$K_{\mu_{\text{dop}}, C_{V\ddot{O},b}}^{IJ} = \int_V \frac{\partial M_{\text{dop}}}{\partial C_{V\ddot{O},b}} N_{C_{V\ddot{O},b}}^J \mu_{\text{dop},i} N_{\mu_{\text{dop},i}}^I dV - \int_{\Gamma} \frac{\partial M_{\text{dop}}}{\partial C_{V\ddot{O},b}} N_{C_{V\ddot{O},b}}^J \mu_{\text{dop},i} N_{\mu_{\text{dop},i}}^I \hat{n}_i d\Gamma \quad (\text{S41})$$

$$K_{\mu_{\text{dop}}, C_{\text{dop},b}}^{IJ} = \int_V \frac{\partial M_{\text{dop}}}{\partial C_{\text{dop},b}} N_{C_{\text{dop},b}}^J \mu_{\text{dop},i} N_{\mu_{\text{dop},i}}^I dV - \int_{\Gamma} \frac{\partial M_{\text{dop}}}{\partial C_{\text{dop},b}} N_{C_{\text{dop},b}}^J \mu_{\text{dop},i} N_{\mu_{\text{dop},i}}^I \hat{n}_i d\Gamma \quad (\text{S42})$$

$$K_{C_{V\ddot{O},b}, C_{V\ddot{O},c}}^{IJ} = \int_V N_{C_{V\ddot{O},b}}^I \left( \frac{\partial^2 \mathcal{F}}{\partial C_{V\ddot{O},b} \partial C_{V\ddot{O},c}} N_{C_{V\ddot{O},c}}^J - \frac{\partial^2 \mathcal{F}}{\partial C_{V\ddot{O},c}^2} N_{C_{V\ddot{O},c}}^J \right) dV \quad (\text{S43})$$

$$K_{C_{V\ddot{O},b}, C_{\text{dop},c}}^{IJ} = \int_V N_{C_{V\ddot{O},b}}^I \left( \frac{\partial^2 \mathcal{F}}{\partial C_{V\ddot{O},b} \partial C_{\text{dop},c}} N_{C_{\text{dop},c}}^J - \frac{\partial^2 \mathcal{F}}{\partial C_{V\ddot{O},c} \partial C_{\text{dop},c}} N_{C_{\text{dop},c}}^J \right) dV \quad (\text{S44})$$

$$K_{C_{V\ddot{O},b}, \eta_i}^{IJ} = \int_V N_{C_{V\ddot{O},b}}^I \left( \frac{\partial^2 \mathcal{F}}{\partial C_{V\ddot{O},b} \partial \eta_i} N_{\eta_i}^J - \frac{\partial^2 \mathcal{F}}{\partial C_{V\ddot{O},c} \partial \eta_i} N_{\eta_i}^J \right) dV \quad (\text{S45})$$

$$K_{C_{V\ddot{O},b}, C_{V\ddot{O},b}}^{IJ} = \int_V N_{C_{V\ddot{O},b}}^I \left( \frac{\partial^2 \mathcal{F}}{\partial C_{V\ddot{O},b}^2} N_{C_{V\ddot{O},b}}^J - \frac{\partial^2 \mathcal{F}}{\partial C_{V\ddot{O},c} \partial C_{V\ddot{O},b}} N_{C_{V\ddot{O},b}}^J \right) dV \quad (\text{S46})$$

$$K_{C_{V\ddot{O},b}, C_{\text{dop},b}}^{IJ} = \int_V N_{C_{V\ddot{O},b}}^I \left( \frac{\partial^2 \mathcal{F}}{\partial C_{V\ddot{O},b} \partial C_{\text{dop},b}} N_{C_{\text{dop},b}}^J - \frac{\partial^2 \mathcal{F}}{\partial C_{V\ddot{O},c} \partial C_{\text{dop},b}} N_{C_{\text{dop},b}}^J \right) dV \quad (\text{S47})$$

$$K_{C_{V\ddot{O},b},\phi}^{IJ} = \int_V N_{C_{V\ddot{O},b}}^I \left( \frac{\partial^2 \mathcal{F}}{\partial C_{V\ddot{O},b} \partial \phi} N_{\phi}^J - \frac{\partial^2 \mathcal{F}}{\partial C_{V\ddot{O},c} \partial \phi} N_{\phi}^J \right) dV \quad (S48)$$

$$K_{C_{\text{dop},b},C_{V\ddot{O},c}}^{IJ} = \int_V N_{C_{\text{dop},b}}^I \left( \frac{\partial^2 \mathcal{F}}{\partial C_{\text{dop},b} \partial C_{V\ddot{O},c}} N_{C_{V\ddot{O},c}}^J - \frac{\partial^2 \mathcal{F}}{\partial C_{\text{dop},c} \partial C_{V\ddot{O},c}} N_{C_{V\ddot{O},c}}^J \right) dV \quad (S49)$$

$$K_{C_{\text{dop},b},C_{\text{dop},c}}^{IJ} = \int_V N_{C_{\text{dop},b}}^I \left( \frac{\partial^2 \mathcal{F}}{\partial C_{\text{dop},b} \partial C_{\text{dop},c}} N_{C_{\text{dop},c}}^J - \frac{\partial^2 \mathcal{F}}{\partial C_{\text{dop},c}^2} N_{C_{\text{dop},c}}^J \right) dV \quad (S50)$$

$$K_{C_{\text{dop},b},\eta_i}^{IJ} = \int_V N_{C_{\text{dop},b}}^I \left( \frac{\partial^2 \mathcal{F}}{\partial C_{\text{dop},b} \partial \eta_i} N_{\eta_i}^J - \frac{\partial^2 \mathcal{F}}{\partial C_{\text{dop},c} \partial \eta_i} N_{\eta_i}^J \right) dV \quad (S51)$$

$$K_{C_{\text{dop},b},C_{V\ddot{O},b}}^{IJ} = \int_V N_{C_{\text{dop},b}}^I \left( \frac{\partial^2 \mathcal{F}}{\partial C_{\text{dop},b} \partial C_{V\ddot{O},b}} N_{C_{V\ddot{O},b}}^J - \frac{\partial^2 \mathcal{F}}{\partial C_{\text{dop},c} \partial C_{V\ddot{O},b}} N_{C_{V\ddot{O},b}}^J \right) dV \quad (S52)$$

$$K_{C_{\text{dop},b},C_{\text{dop},b}}^{IJ} = \int_V N_{C_{\text{dop},b}}^I \left( \frac{\partial^2 \mathcal{F}}{\partial C_{\text{dop},b}^2} N_{C_{\text{dop},b}}^J - \frac{\partial^2 \mathcal{F}}{\partial C_{\text{dop},c} \partial C_{\text{dop},b}} N_{C_{\text{dop},b}}^J \right) dV \quad (S53)$$

$$K_{C_{\text{dop},b},\phi}^{IJ} = \int_V N_{C_{\text{dop},b}}^I \left( \frac{\partial^2 \mathcal{F}}{\partial C_{\text{dop},b} \partial \phi} N_{\phi}^J - \frac{\partial^2 \mathcal{F}}{\partial C_{\text{dop},c} \partial \phi} N_{\phi}^J \right) dV \quad (S54)$$

$$K_{\phi,C_{V\ddot{O},c}}^{IJ} = - \int_V N_{\phi}^I \frac{\mathcal{F}}{V_m} \left( z_{V\ddot{O}} \frac{\partial C_{V\ddot{O}}}{\partial C_{V\ddot{O},c}} N_{V\ddot{O},c}^J \right) dV \quad (S55)$$

$$K_{\phi,C_{\text{dop},c}}^{IJ} = - \int_V N_{\phi}^I \frac{\mathcal{F}}{V_m} \left( z_{\text{dop}} \frac{\partial C_{\text{dop}}}{\partial C_{\text{dop},c}} N_{\text{dop},c}^J \right) dV \quad (S56)$$

$$K_{\phi,\eta_i}^{IJ} = - \int_V N_{\phi}^I \frac{\mathcal{F}}{V_m} \left( z_{V\ddot{O}} \frac{\partial C_{V\ddot{O}}}{\partial \eta_i} N_{\eta_i}^J + z_{\text{dop}} \frac{\partial C_{\text{dop}}}{\partial \eta_i} N_{\eta_i}^J \right) dV \quad (S57)$$

$$K_{\phi,C_{V\ddot{O}}}^{IJ} = - \int_V N_{\phi}^I \frac{\mathcal{F}}{V_m} z_{V\ddot{O}} N_{V\ddot{O}}^J dV \quad (S58)$$

$$K_{\phi,C_{\text{dop}}}^{IJ} = - \int_V N_{\phi}^I \frac{\mathcal{F}}{V_m} z_{\text{dop}} N_{\text{dop}}^J dV \quad (S59)$$

$$K_{\phi,C_{V\ddot{O},b}}^{IJ} = - \int_V N_{\phi}^I \frac{\mathcal{F}}{V_m} \left( z_{V\ddot{O}} \frac{\partial C_{V\ddot{O}}}{\partial C_{V\ddot{O},b}} \right) dV \quad (S60)$$

$$K_{\phi,C_{\text{dop},b}}^{IJ} = - \int_V N_{\phi}^I \frac{\mathcal{F}}{V_m} \left( z_{\text{dop}} \frac{\partial C_{\text{dop}}}{\partial C_{\text{dop},b}} \right) dV \quad (S61)$$

$$K_{\phi,\phi}^{IJ} = \int_V \epsilon_0 \epsilon_r N_{\phi,i}^J N_{\phi,i}^I dV - \int_{\Gamma} \epsilon_0 \epsilon_r N_{\phi,i}^J N_{\phi}^I \hat{n}_i d\Gamma. \quad (S62)$$

## References

- [1] Roger A De Souza. The formation of equilibrium space-charge zones at grain boundaries in the perovskite oxide  $\text{SrTiO}_3$ . *Phys. Chem. Chem. Phys.*, 11(43):9939–9969, 2009.